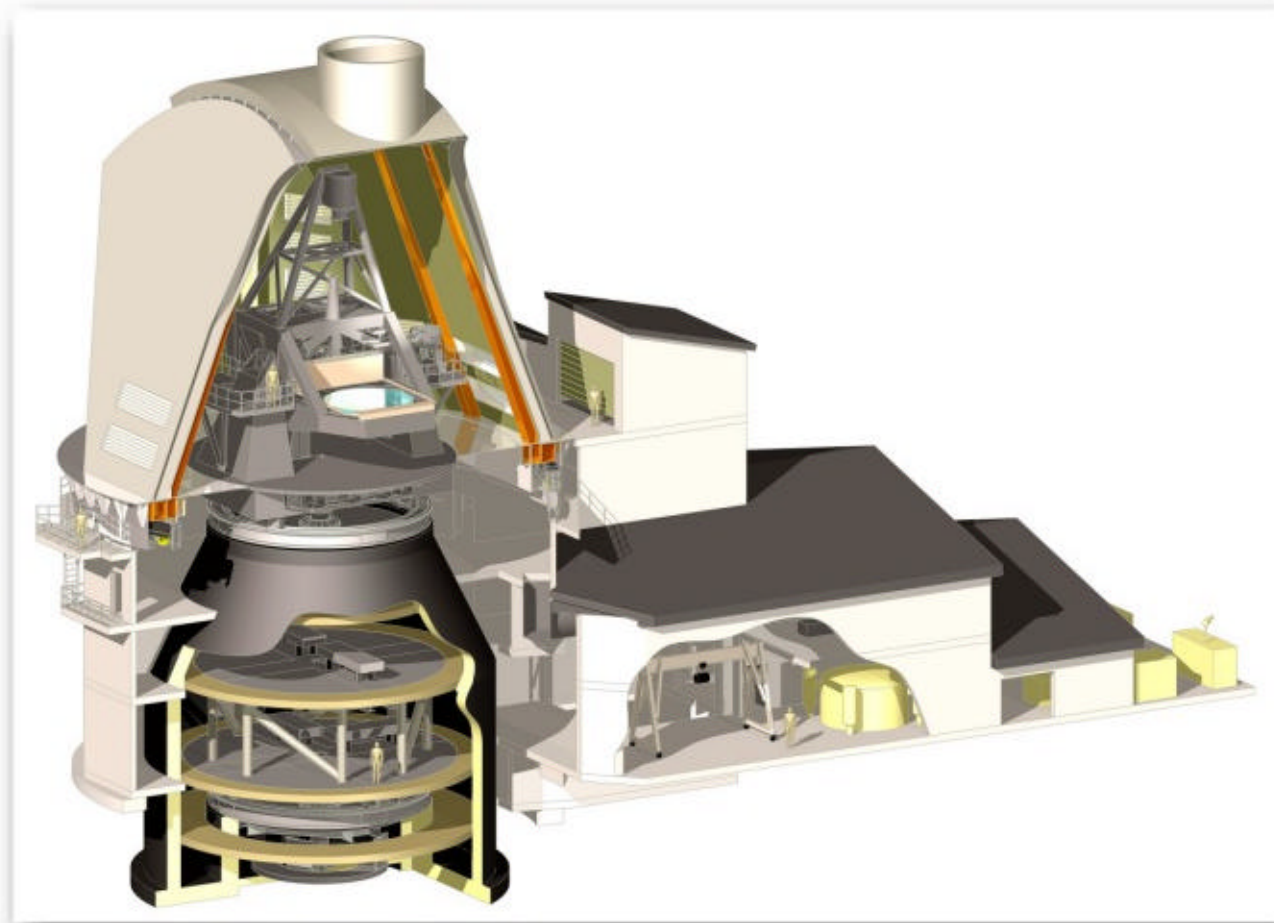


Deriving $C_n^2(h)$ from a Scintillometer Array



F. Hill, R. Radick, and M. Collados

23 April 2003

Revision Summary:

1. Date: 23 April 2003
Revision: A
Changes: Initial Release
2. Date:
Revision:
Changes:
3. Date:
Revision:
Changes:

Table Of Contents

1. INTRODUCTION.....	1
2. BASIC THEORY	2
2.1 Definitions and Assumptions	2
2.2 The Effect of a Thin Turbulent Layer.....	2
2.3 Scintillation Measurements	5
2.4 The Extended-Source Solar Case.....	5
2.5 Properties of the Kernels.....	10
3. DETERMINING $C_n^2(h)$	12
3.1 Model of $C_n^2(h)$	12
3.2 Estimating $C_n^2(h)$	17
4. TESTING THE METHOD.....	18
4.1 Constructing Simulated Profiles of $C_n^2(h)$	18
4.2 Observational Multi-Height Test	19
5. APPLYING THE METHOD TO SAMPLE DATA	22
6. CONCLUSIONS	25
APPENDIX A – THE IDL DATA PREPROCESSING PROCEDURE	31
APPENDIX B – THE IDL KERNEL GENERATING PROCEDURE	33
APPENDIX C – THE IDL INVERSION PROCEDURE	35
APPENDIX D – THE IDL MINIMIZATION FUNCTION PROCEDURE.....	39
REFERENCES	40

Deriving $C_n^2(h)$ from a Scintillometer Array

Frank Hill

Richard Radick

Manuel Collados

April 23, 2003

1. Introduction

It has been known for some time (e.g. Roddier 1981) that the scintillation of starlight is a measure of optical seeing in the atmosphere. Seykora (1993) demonstrated that the scintillation of sunlight is also closely correlated with seeing, providing a simple way to measure seeing in the daytime. Beckers (1993) placed the observation on a firm theoretical basis and also showed (Beckers et al. 1997) that the pattern of decreasing cross-correlation with increasing separation measured by a linear array of scintillometers contains information on the structure function, $C_n^2(h)$. Beckers further developed the idea for solar site testing (Beckers et al. 1997; Beckers and Rutten 1998; Beckers 1999; Beckers 2001; Beckers et al. 2003) into an instrument known as a SHABAR. SHABAR stands for SHAdow BAnd Ranging, and the instrument consists of a non-redundant linear array of six scintillometers.

In this report we present a method to extract $C_n^2(h)$ from the ATST SHABAR instrument. The original method of Beckers (2001) relied on a specific model (Huffnagel-Valley) of $C_n^2(h)$ and estimated a few parameters from the data. The assumption of a specific model can lead to errors when nature does not cooperate. A method developed by R. Radick (Radick et al. 2002) extended the original method and dispensed with adopting a pre-determined $C_n^2(h)$. Radick demonstrated that the data can be used to detect the general characteristics of $C_n^2(h)$ by comparing observations obtained at three heights. Here we present a more detailed inversion of the data that produces a quantitative estimate of $C_n^2(h)$ and thus allows the determination of r_0 as a function of height. We follow the approach developed by Hickson & Lanzetta as presented in their draft manuscript “Measurement of atmospheric turbulence and wind profiles with a scintillometer array”, to be submitted to *PASP*, 2002 (referred to as paper HL).

We present the method in considerable detail to allow implementation by interested researchers and review by the ATST SSWG. We test the methods with simulated data and also compare the results of the analyses using the “Three-Height” data obtained at Sacramento Peak in November, 2001.

2. Basic Theory

In this section we summarize the relevant portions of the basic theory of wave propagation in a turbulent medium, using the formalism of sections 3.1, 7, and 8 of Roddier (1981).

2.1 Definitions and Assumptions

Following section 3.1 of Roddier (1981), consider a monochromatic horizontal plane wave of wavelength λ propagating through the atmosphere with a coordinate system described by a vertical height h above the ground and a horizontal position denoted by a coordinate vector \mathbf{x} . The wave field in the atmosphere can then be written as a complex amplitude $\Psi_h(\mathbf{x})$ with

$$\Psi_h(\mathbf{x}) = |\Psi_h(\mathbf{x})| \exp [\phi_h(\mathbf{x})] \quad (1)$$

At each height, the phase $\phi_h(\mathbf{x})$ is taken with respect to its average value so that for any h , $\langle \phi_h(\mathbf{x}) \rangle = 0$ where the angle brackets indicate that an average (in this case over all horizontal directions) has been taken. The unperturbed complex amplitude of the wave is normalized to unity outside the atmosphere so that $\Psi_\infty(\mathbf{x}) = 1$. The atmosphere is assumed to be non-absorbing and horizontally stratified so that its statistical properties depend only on h .

2.2 The Effect of a Thin Turbulent Layer

Assume that the wave propagates vertically downward at the zenith through a thin horizontal turbulent layer between height h and $h + \delta h$. The thickness δh is assumed to be large compared to the correlation scale of the layer inhomogeneities but small enough so that diffraction over δh can be ignored. At the top of the layer, the normalization and assumptions discussed above give $\Psi_{h+\delta h}(\mathbf{x}) = 1$. At the bottom of the layer,

$$\Psi_h(\mathbf{x}) = \exp [\phi(\mathbf{x})] \quad (2)$$

where $\phi(\mathbf{x})$ is the phase shift created by refraction of index fluctuations $n(\mathbf{x}, h)$ in the layer:

$$\phi(\mathbf{x}) = \frac{2\pi}{\lambda} \int_h^{h+\delta h} n(\mathbf{x}, h') dh' \quad (3)$$

From the bottom of the layer to the ground at $h = 0$, the propagation of the wave can be described by Fresnel diffraction. Thus,

$$\Psi_0(\mathbf{x}) = \Psi_h(\mathbf{x}) * \frac{1}{i\lambda h} \exp \left(i\pi \frac{\mathbf{x}^2}{\lambda h} \right) \quad (4)$$

where the symbol $*$ indicates convolution.

As discussed in section 7 of Roddier (1981), the small perturbation assumption can usually, but not always, be made for astronomical observations at zenith angles $\zeta < 60^\circ$. This assumption is

that $\phi(\mathbf{x}) \ll 1$ and thus $\Psi_h(\mathbf{x}) \approx 1 + i\phi(\mathbf{x})$. Note that this is a fairly restrictive assumption that, if violated, invalidates the representation of continuous turbulence as a linear sum of the contributions from many individual thin layers. With the small perturbation assumption,

$$\Psi_0(\mathbf{x}) = [1 + i\phi(\mathbf{x})] * \frac{1}{i\lambda h} \exp\left(i\pi \frac{\mathbf{x}^2}{\lambda h}\right) \quad (5)$$

It can be shown that

$$1 * \frac{1}{i\lambda h} \exp\left(i\pi \frac{\mathbf{x}^2}{\lambda h}\right) = 1 \quad (6)$$

so that

$$\Psi_0(\mathbf{x}) = 1 + \epsilon(\mathbf{x}) \quad (7)$$

where

$$\epsilon(\mathbf{x}) = \phi(\mathbf{x}) * \frac{1}{\lambda h} \exp\left(i\pi \frac{\mathbf{x}^2}{\lambda h}\right) \quad (8)$$

is the relative fluctuation of the complex amplitude of the wave at the ground.

The real part of $\epsilon(\mathbf{x})$

$$\chi(\mathbf{x}) = \phi(\mathbf{x}) * \frac{1}{\lambda h} \cos\left(\pi \frac{\mathbf{x}^2}{\lambda h}\right) \quad (9)$$

represents the fluctuations of the modulus $|\Psi_0(\mathbf{x})|$ while the imaginary part

$$\phi_0(\mathbf{x}) = \phi(\mathbf{x}) * \frac{1}{\lambda h} \sin\left(\pi \frac{\mathbf{x}^2}{\lambda h}\right) \quad (10)$$

represents the phase fluctuations.

The spatial covariance of the amplitude and phase fluctuations can be written as

$$B_\chi(\mathbf{r}) = \langle \chi(\mathbf{x}) \chi(\mathbf{x} + \mathbf{r}) \rangle \quad (11)$$

$$B_{\phi_0}(\mathbf{r}) = \langle \phi_0(\mathbf{x}) \phi_0(\mathbf{x} + \mathbf{r}) \rangle \quad (12)$$

where the angle brackets denote an average over \mathbf{x} . The Fourier transforms of B_χ and B_{ϕ_0} are the power spectra $W_\chi(\mathbf{f})$ and $W_{\phi_0}(\mathbf{f})$ of the amplitude and phase fluctuations, where \mathbf{f} is the two-dimensional spatial frequency in units of inverse length. Explicitly,

$$W_\chi = \int B_\chi(\mathbf{r}) \exp(-2\pi \mathbf{r} \cdot \mathbf{f}) d\mathbf{r} = W_\phi(\mathbf{f}) \sin^2(\pi \lambda h \mathbf{f}^2) \quad (13)$$

$$W_{\phi_0} = W_\phi(\mathbf{f}) \cos^2(\pi \lambda h \mathbf{f}^2) \quad (14)$$

where $W_\phi(\mathbf{f})$ is the two-dimensional power spectrum of the complex phase fluctuations at the bottom of the layer. In general, $W_\phi(\mathbf{f})$ is related to the three-dimensional power spectrum of refractive index fluctuations, Φ_n , by

$$W_\phi(\mathbf{f}) = \left(\frac{2\pi}{\lambda}\right)^2 \delta h (2\pi)^3 \Phi_n(2\pi\mathbf{f}) \quad (15)$$

For Kolmogorov turbulence,

$$\Phi_n(k) = 0.033 C_n^2(h) k^{-11/3} \quad (16)$$

where k is the magnitude of the spatial wavenumber, $k = 2\pi f = 2\pi |\mathbf{f}|$. Combining terms, the expressions for the two-dimensional power spectrum of amplitude and phase fluctuations arising from a single thin layer at height h and thickness δh are

$$W_\chi(\mathbf{f}) = 0.38 \lambda^{-2} f^{-11/3} C_n^2(h) \delta h \sin^2(\pi \lambda h f^2) \quad (17)$$

$$W_{\phi_0}(\mathbf{f}) = 0.38 \lambda^{-2} f^{-11/3} C_n^2(h) \delta h \cos^2(\pi \lambda h f^2) \quad (18)$$

It is useful to summarize the major assumptions that have been made in the theory. First, for the small perturbation approximation ($\phi(\mathbf{x}) \ll 1$), fluctuations produced by several layers add linearly. Since the layer properties are statistically independent, their power spectra also add linearly, and any continuous distribution of turbulence will produce power spectra of the form

$$W_\chi(\mathbf{f}) = 0.38 \lambda^{-2} f^{-11/3} \int C_n^2(h) \sin^2(\pi \lambda h f^2) dh \quad (19)$$

$$W_{\phi_0}(\mathbf{f}) = 0.38 \lambda^{-2} f^{-11/3} \int C_n^2(h) \cos^2(\pi \lambda h f^2) dh \quad (20)$$

This is vital for the determination of $C_n^2(h)$. The small perturbation approximation usually holds if the zenith angle, ζ , is less than 60° , but occasionally breaks down even for moderate ζ . In addition, the small perturbation approximation can be valid at large zenith angles. The scintillation saturates when the approximation is invalid. It would be useful to have an observable way of continuously determining the validity of the approximation.

The other major assumptions concern the turbulent power spectrum. The first is that the turbulent spectrum is Kolmogorov, i.e. both the power spectrum of temperature fluctuations $\Phi_T(k)$ and humidity fluctuations $\Phi_C(k)$ are proportional to $k^{-5/3}$. This may not always be true, especially if the inner and outer scales (the minimum and maximum length scales between which the spectrum actually is Kolmogorov) are on the order of the relevant dimensions of the observing system. In addition, the structure function $C_n^2(h)$ is assumed to depend only on the temperature fluctuations without any contributions from humidity fluctuations. This may not be true in the vicinity of a lake.

2.3 Scintillation Measurements

The ATST SHABAR system measures the scintillation index, σ_I^2 , defined as the variance of the relative irradiance fluctuations. The scintillation index is related to the variance σ_χ^2 of the relative amplitude fluctuations by

$$\sigma_I^2 = 4\sigma_\chi^2 \quad (21)$$

and the spatial power spectrum of scintillation, $W_I(\mathbf{f})$, is related to $W_\chi(\mathbf{f})$ by

$$W_I(\mathbf{f}) = 4W_\chi(\mathbf{f}) = 1.52\lambda^{-2}f^{-11/3} \delta h C_n^2(h) \sin^2(\pi\lambda h f^2) \quad (22)$$

for a single layer, and

$$W_I(\mathbf{f}) = 4W_\chi(\mathbf{f}) = 1.52\lambda^{-2}f^{-11/3} \int C_n^2(h) \sin^2(\pi\lambda h f^2) dh \quad (23)$$

for a continuous distribution of turbulence.

Figure 1 shows plots of the single-layer $W_I(\mathbf{f})$ per unit height for five heights H assuming that 1) $C_n^2(H) = 10^{-13}$, and is independent of H ; 2) the object is at the zenith; and 3) the ATST SHABAR has a wavelength coverage centered on 510 nm. The spatial covariance $B(x)$, where x is distance, is the real part of the Fourier transform of $W_I(\mathbf{f})$. Figure 2 shows this function corresponding to the power spectra in Figure 1. The ATST SHABAR measures $B(x)$ but, since the sun is an extended source rather than a point source, the shape of the function $B(x)$ is rather different. This shape is derived in the next section.

2.4 The Extended-Source Solar Case

So far, these equations have been developed for scintillation of a point source at the zenith observed with an infinitely small detector. Since the sun is an extended source, the SHABAR detectors have a finite size, and the sun is almost never at the zenith, the equations must be generalized. Much of the following development can be found in Hickson & Lanzetta (2002)

The generalization to $\zeta \neq 0$ is simple. Since the diffraction from the layer depends on distance from the layer, replacing h in the diffraction term with the line-of-sight distance to the layer, $z = h \sec \zeta$, transforms the amplitude power spectrum into the non-zenith form:

$$W_\chi(\mathbf{f}) = 0.38 \sec \zeta \lambda^{-2} f^{-11/3} \int C_n^2(h) \sin^2(\pi\lambda z f^2) dh \quad (24)$$

where the $\sec \zeta$ term before the integral comes from $dz = dh \sec \zeta$.

Generalizing the power spectrum to the case of an extended source and detector is somewhat more involved. Assuming that both the source and the detector are circular, Figure 3 shows the geometry of the beams defined by the source, the detector, and the height of the turbulence. Following Figure 3, θ is the angular diameter of the source, then define $\alpha = 2 \tan(\theta/2)$. For the

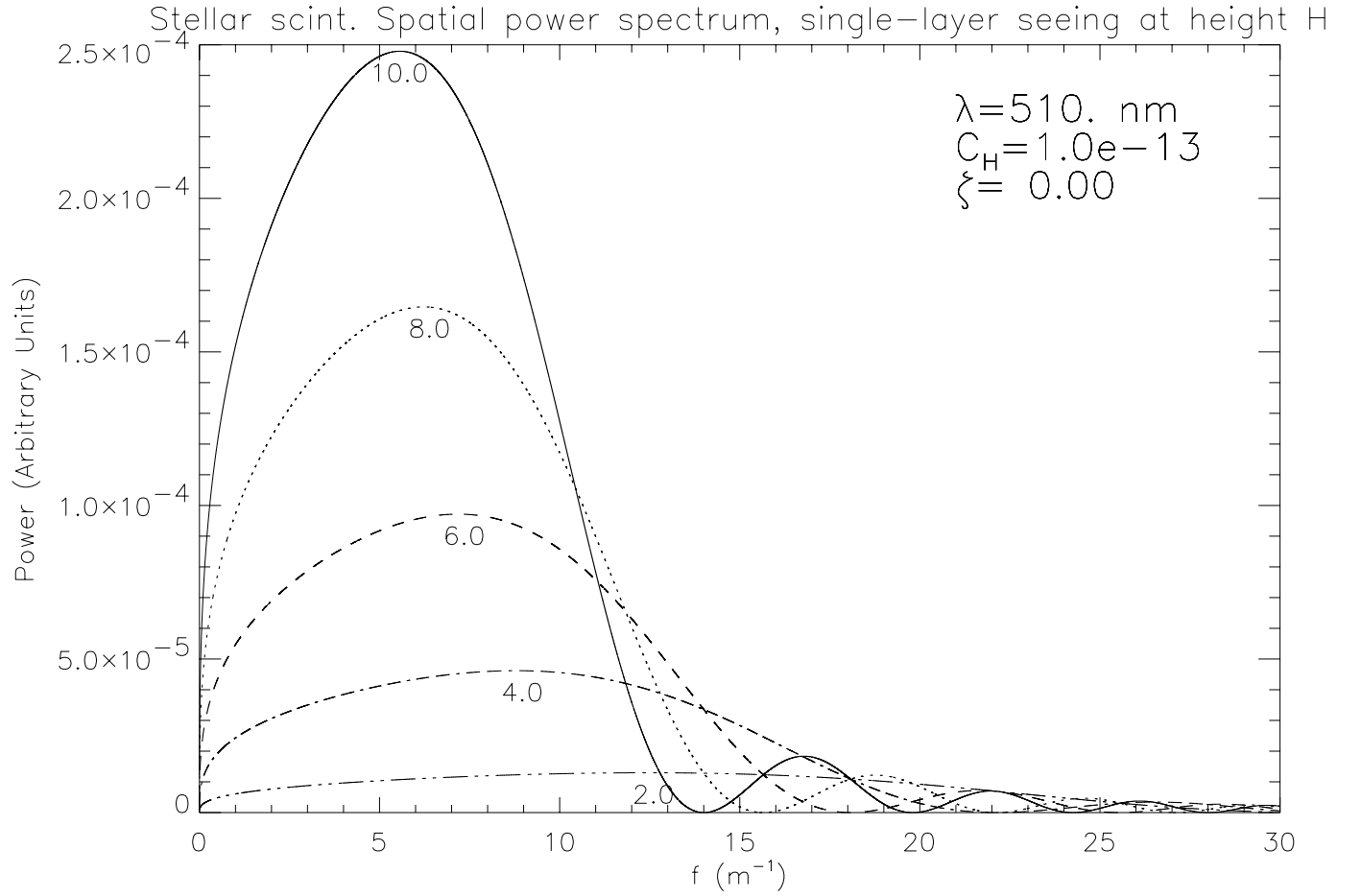


Fig. 1 The spatial power spectrum of the stellar scintillation signal that would result from single-layer seeing at the heights indicated in km.

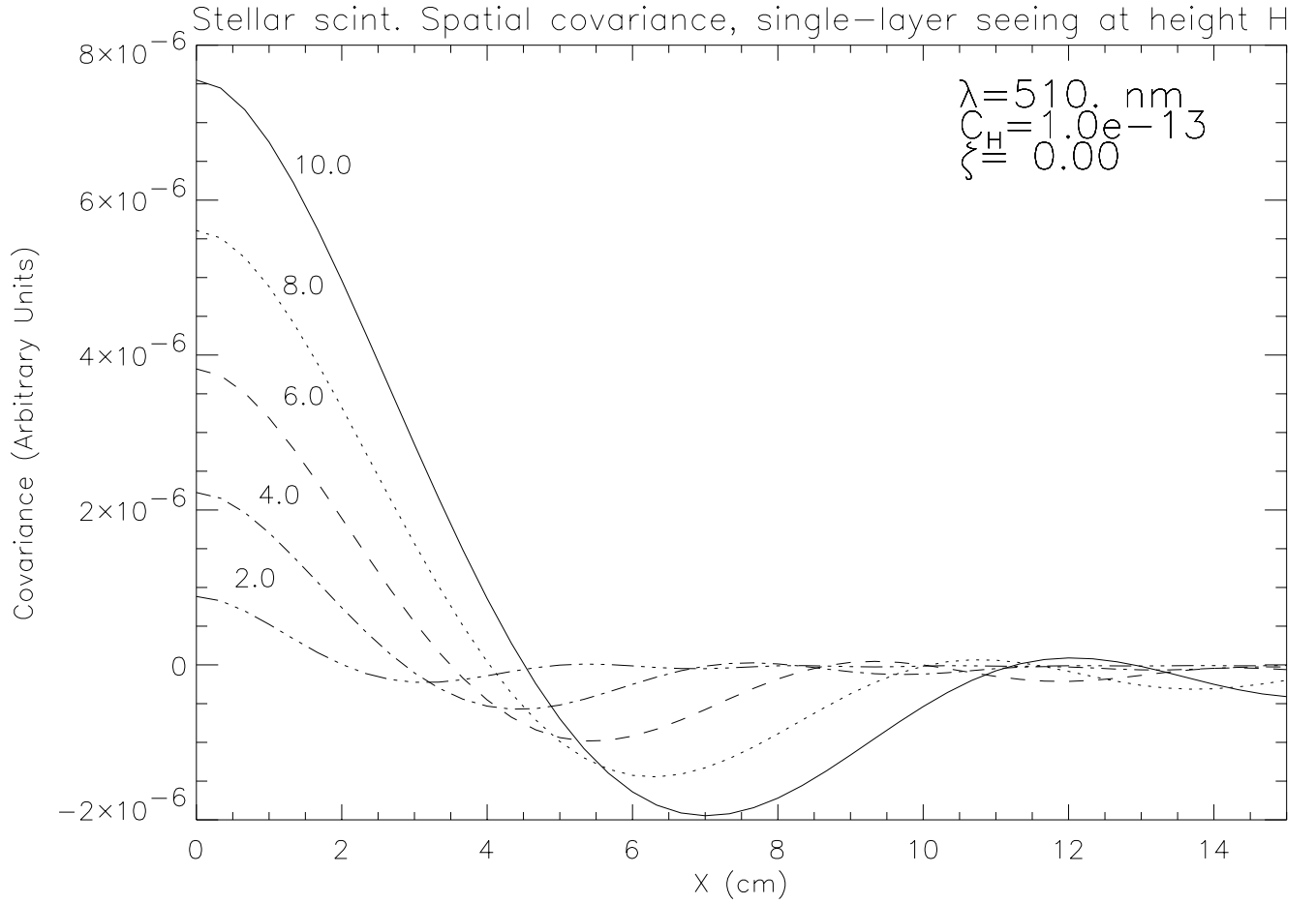


Fig. 2 The spatial covariance of the stellar scintillation signal that would result from single-layer seeing at the heights indicated.

small angular diameter of the sun, $\alpha \approx \theta$. Then, with detectors of diameter a , at height h the rays propagating from the source to the detector pass through an area $\mathbf{A}(\mathbf{x}, z)$ perpendicular to the line of sight with

$$\mathbf{A}(\mathbf{x}, z) = \Pi\left(\frac{x}{a + \alpha z}\right) \quad (25)$$

where

$$\Pi(x) = \begin{cases} 1 & x \leq 1/2 \\ 0 & x > 1/2 \end{cases} \quad (26)$$

The term in the denominator, $a + \alpha z$, is the diameter of the cone defined by θ and a at the line of sight distance $z = h \sec \zeta$.

Thus, the complex wave amplitude $\Psi(\mathbf{x}, z)$ resulting from the turbulence at height h is averaged over the area of the beam. This average amplitude, $\langle \Psi(\mathbf{x}, z) \rangle$, can be written as a convolution with the normalized area $\mathcal{A}(\mathbf{x}, z)$:

$$\langle \Psi(\mathbf{x}, z) \rangle = \Psi(\mathbf{x}, z) * \mathcal{A}(\mathbf{x}, z) = \Psi(\mathbf{x}, z) * \frac{4\mathbf{A}(\mathbf{x}, z)}{\pi(a + \alpha z)^2} \quad (27)$$

Replacing $\Psi(\mathbf{x}, z)$ with $\langle \Psi(\mathbf{x}, z) \rangle$ in the derivation in Section 2.2 leads to convolving $\phi(\mathbf{x}, z)$ with $\mathcal{A}(\mathbf{x}, z)$ and thus the covariance function $B_\chi(\mathbf{r})$ will contain the factor $\mathcal{A}(\mathbf{x}, z) * \mathcal{A}(\mathbf{x}, z)$. From the convolution theorem for Fourier transforms, the power spectrum $W_\chi(\mathbf{f})$ will then be multiplied by the squared modulus of the two-dimensional Fourier transform of $\mathcal{A}(\mathbf{x}, z)$ denoted as $\mathcal{G}(\mathbf{f}, z)$:

$$W_\chi(\mathbf{f}) = 0.38 \sec \zeta \lambda^{-2} f^{-11/3} \int C_n^2(h) \mathcal{G}(\mathbf{f}, z) \sin^2(\pi \lambda z f^2) dh \quad (28)$$

where

$$\mathcal{G}(\mathbf{f}, z) = \left| \int \int \mathcal{A}(\mathbf{x}, z) \exp(-2\pi i \mathbf{x} \cdot \mathbf{f}) d^2 x \right|^2 \quad (29)$$

$$= \left[\frac{2J_1(\pi(a + \alpha z)f)}{\pi(a + \alpha z)f} \right]^2 \quad (30)$$

where J_1 is the first-order Bessel function of the first kind.

Since the spatial covariance $B_\chi(\mathbf{r})$ is the inverse Fourier transform of the spatial power spectrum $W_\chi(\mathbf{f})$ and the spatial covariance of the intensity fluctuations $B_I(\mathbf{r}) = 4B_\chi(\mathbf{r})$, then

$$B_I(r) = 0.38 \int_0^\infty C_n^2(h) K(h, r) dh \quad (31)$$

where the kernel function $K(h, r)$ is given by

$$K(h, r) = 8\pi \sec \zeta \lambda^{-2} \int_0^\infty \sin^2(\pi \lambda h \sec \zeta f^2) \mathcal{G}(f, h \sec \zeta) J_0(2\pi f r) f^{-8/3} df \quad (32)$$

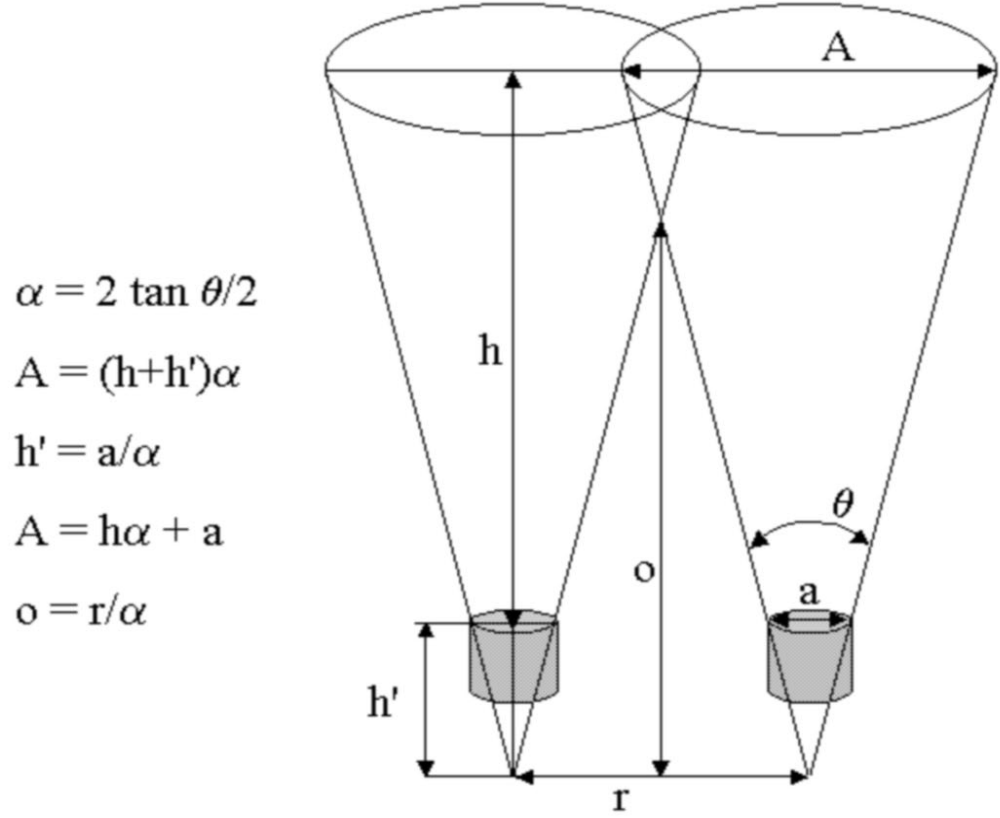


Fig. 3 The geometry of the beams defined by the source and detectors intersecting the turbulence. The symbols are: θ , angular diameter of the source (i.e. the sun); a , the linear diameter of the detector; r , the separation of the detectors; h , the height of the turbulence; A , the linear diameter of the cone at h ; h' , the distance behind the detector at which the cone converges; o , the height at which the cones from the two detectors intersect; and $\alpha = 2 \tan \theta/2 \approx \theta$.

where J_0 is the zeroth-order Bessel function of the first kind.

A plot of $\mathcal{G}(\mathbf{f}, z)$ shows that it essentially reaches zero and thus truncates the integral when $f > (a + \alpha z)^{-1}$. Therefore, the argument of the sine must be less than $\pi \lambda z / (a + \alpha z)^2$. Taking the derivative of this function and setting it equal to zero shows that the argument reaches a maximum at $z = a/\alpha$, at which point the value is $\pi \lambda / 4a\alpha$. For the SHABAR, with $a = 0.002$ m, $\alpha > .009$, and $\lambda = 500$ nm, the maximum value of the argument is about 0.02 and the sine can be approximated by its argument. Thus,

$$K(h, r) = 8\pi^3 h^2 \sec^3 \zeta \int_0^\infty \mathcal{G}(f, h \sec \zeta) J_0(2\pi f r) f^{4/3} df \quad (33)$$

$$= \frac{32\pi h^2 \sec^3 \zeta}{(a + \alpha h \sec \zeta)^2} \int_0^\infty [J_1(\pi(a + \alpha h \sec \zeta)f)]^2 J_0(2\pi f r) f^{-2/3} df \quad (34)$$

With a change of variables from f to $(a + \alpha h \sec \zeta)f$, this can be written as

$$K(h, r) = \frac{32\pi h^2 \sec^3 \zeta}{(a + \alpha h \sec \zeta)^{7/3}} Q\left(\frac{r}{a + \alpha h \sec \zeta}\right) \quad (35)$$

where

$$Q(s) = \int_0^\infty [J_1(\pi f)]^2 J_0(2\pi f s) f^{-2/3} df \quad (36)$$

2.5 Properties of the Kernels

Figure 4 shows the function $Q(s)$, which depends on the detector separation r scaled by a factor $a + \alpha h \sec \zeta$. This factor contains geometry effects: the diameter of the detector a , and the temporally varying effects of the solar radius θ ($\alpha = 2 \tan(\theta/2)$), and the zenith angle, ζ .

Figure 5 shows $0.38 * K(h, r)$ as a function of $\log(h)$ for the fifteen SHABAR separations at $\zeta = 0^\circ$, $\theta = 960.0$ arcsec, and for the SHABAR detector diameters of 2 mm. This plot provides some qualitative feel for the height range of the SHABAR. The curves are distinct below about 1000 m, so the maximum height of sensitivity of the system is roughly $1000 \cos \zeta$ meters. In addition the curves are slightly negative, indicating that the covariances could also become negative (i.e. anticorrelation could occur) if the turbulence has significant structure close to the ground. Figure 6 shows $0.38 * K(h, r)$ as a function of r for selected heights. This figure illustrates the decrease in signal as the height of the turbulence increases.

Figures 7 and 8 show the effect of the temporal variations of θ and ζ during the measurements. These variations effectively change the area over which the turbulence power spectrum is measured. This changes the apparent spatial spectrum by truncating the wavenumber response of the measurement. Figure 7 shows the effect of the variation in the apparent solar diameter during the course of the year. This effect is rather small in magnitude, about 5 %. However, Figure 8 shows the importance of including the zenith angle ζ in the computation of $K(h, r)$. The change in the

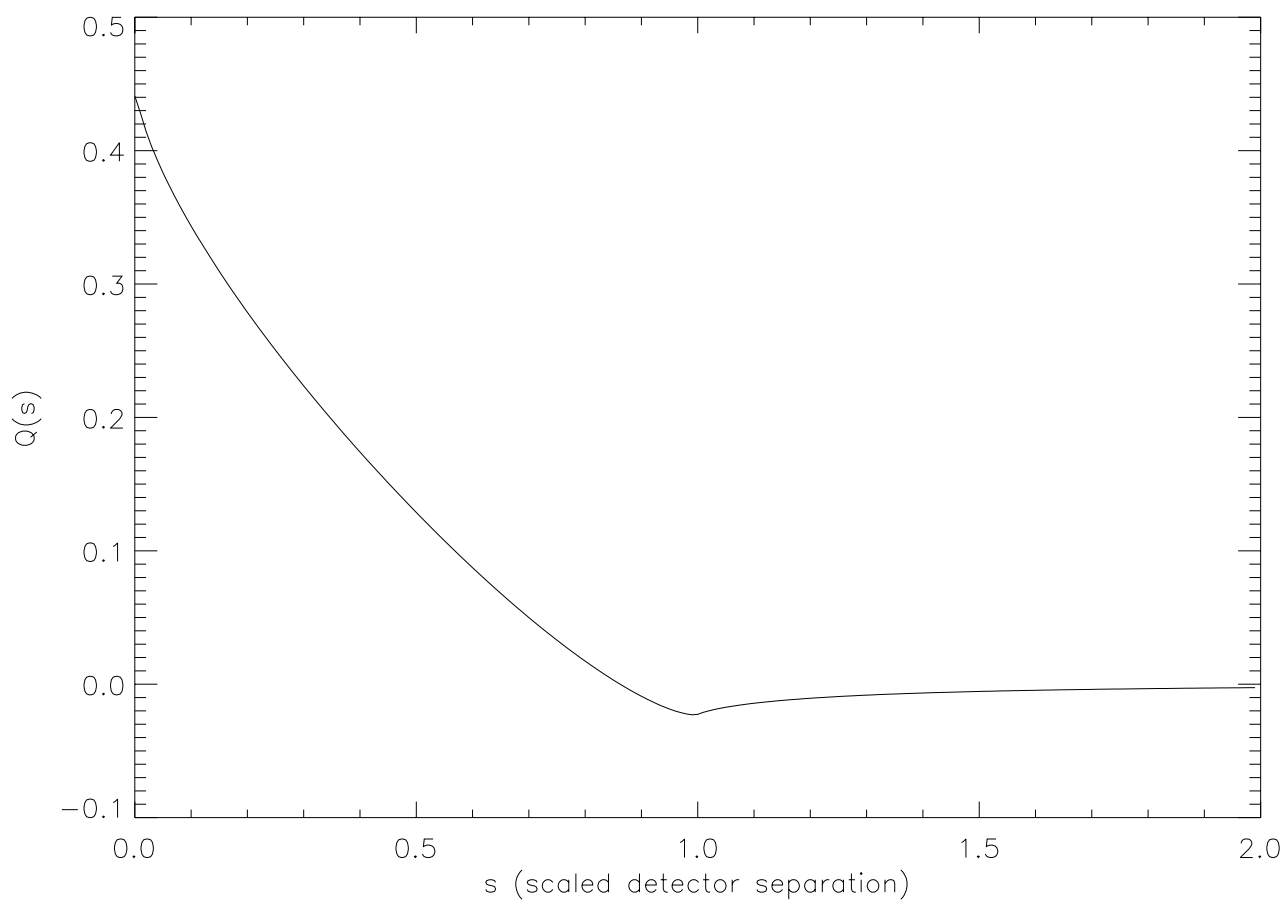


Fig. 4 The function $Q(s)$.

curves is quite large, and increases rapidly with increasing ζ . This is primarily due to the ζ terms in the expression for $K(h, r)$.

3. Determining $C_n^2(h)$

The basic equation for the method is the spatial covariance of the intensity fluctuation given by

$$B_I(r) = 0.38 \int_0^\infty C_n^2(h) K(h, r) dh \quad (37)$$

where the kernel $K(h, r)$ is

$$K(h, r) = \frac{32\pi h^2 \sec^3 \zeta}{(a + \alpha h \sec \zeta)^{7/3}} Q\left(\frac{r}{a + \alpha h \sec \zeta}\right) \quad (38)$$

In practice, we have the measurements $B_I(r)$, can calculate the kernels $K(h, r)$, and seek estimates of $C_n^2(h)$. This is a classic inversion problem of the type encountered in radiative transfer, vector magnetometry, and helioseismology. Many methods have been developed to solve this problem. Here we describe the solution adopted for the SHABAR, which corresponds to the method of regularized least squares.

3.1 Model of $C_n^2(h)$

The covariance $B_I(r)$ is sampled by a non-redundant array of six detectors, giving 15 different baselines. The 15 covariance values are recorded every 10 seconds by the SHABAR. Let n be the number of baselines ($n = 15$ for the SHABAR), r_j be the lengths of the baselines, and B_j the measured covariances over the baselines. Further, model $C_n^2(h)$ as an expansion in a set of m basis functions $\mathcal{C}_i(h)$ so that

$$C_n^2(h) = \sum_{i=1}^m a_i \mathcal{C}_i(h) \quad (39)$$

There are many choices for $\mathcal{C}_i(h)$. Here we select Dirac delta functions as the simplest option. Then,

$$\mathcal{C}_i(h) = \delta(h - h_i) \quad (40)$$

Next, define

$$K_{ij} = 0.38 \int_0^\infty \mathcal{C}_i(h) K(h, r_j) dh \quad (41)$$

Then, with this model,

$$B_I(r_j) = \sum_{i=0}^m a_i K_{ij} \quad (42)$$

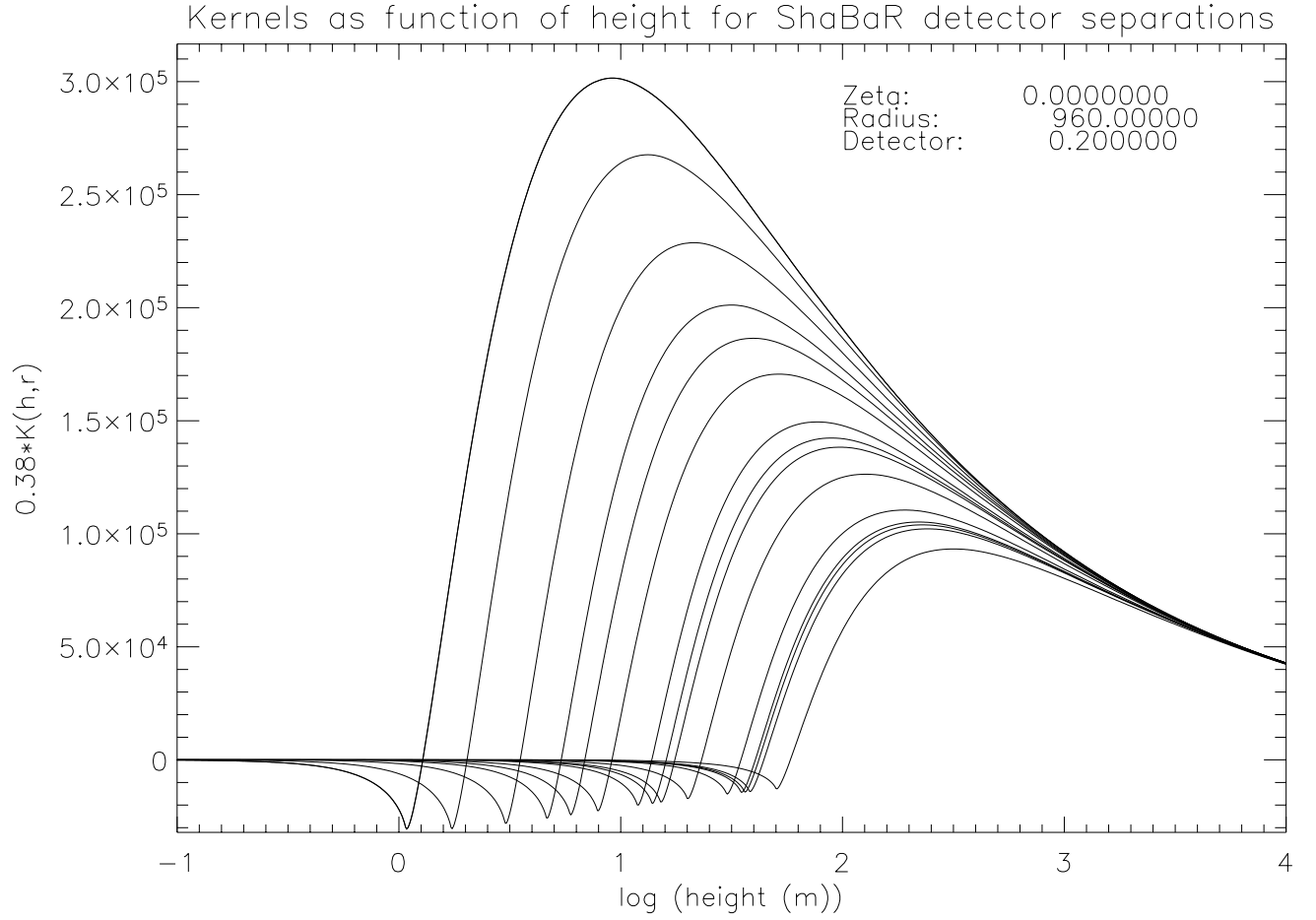


Fig. 5 The functions $0.38K(h, r)$ as a function of $\log(h)$ for the SHABAR detector separations. These curves are for $\theta = 960$ arcsec, $\zeta = 0^\circ$, and $a = 0.2$ cm.

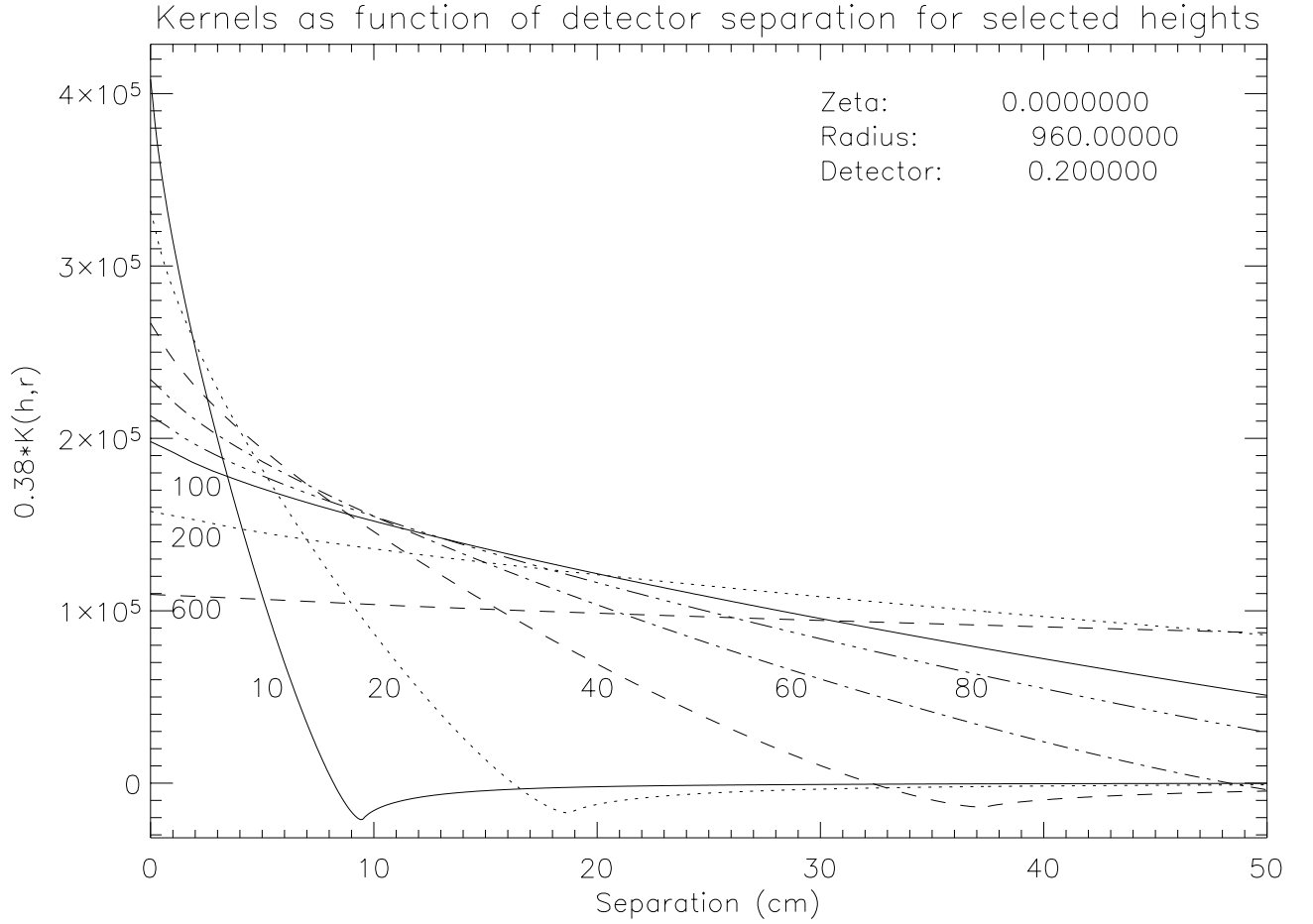


Fig. 6 The functions $0.38K(h, r)$ as a function of separation r for the the heights 10, 20, 40, 60, 80, 100, 200, and 600 meters. These curves are for $\theta = 960$ arcsec, $\zeta = 0^\circ$, and $a = 0.2$ cm.

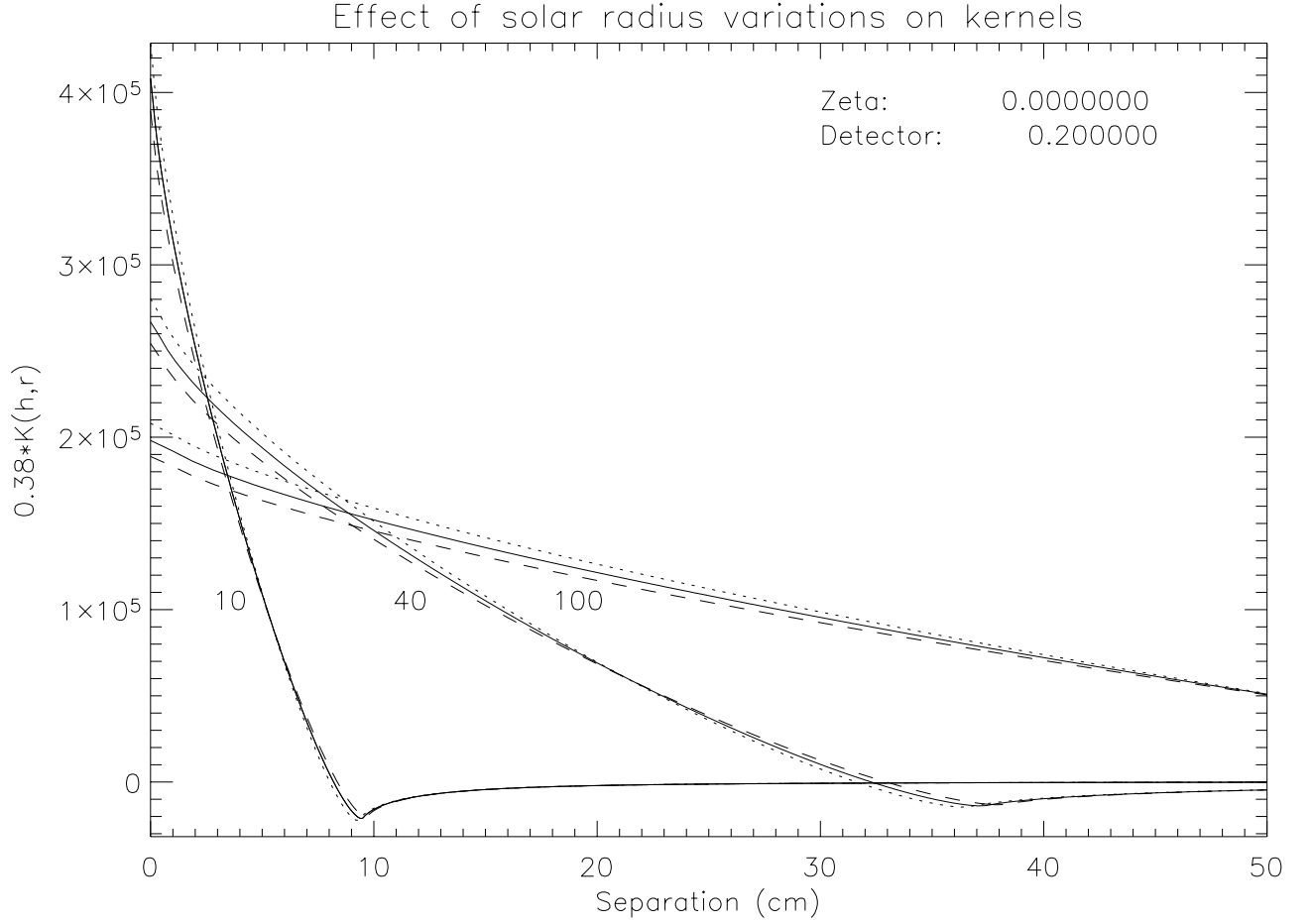


Fig. 7 The effect of the changing apparent solar diameter on $0.38K(h, r)$. The function is shown for $\theta = 940$ arcsec (dashed lines), 960 arcsec (solid lines) and 980 arcsec (dotted lines) at three heights (10, 40, and 100 m). For this plot, $\zeta = 0^\circ$; and $a = 0.2$ cm.

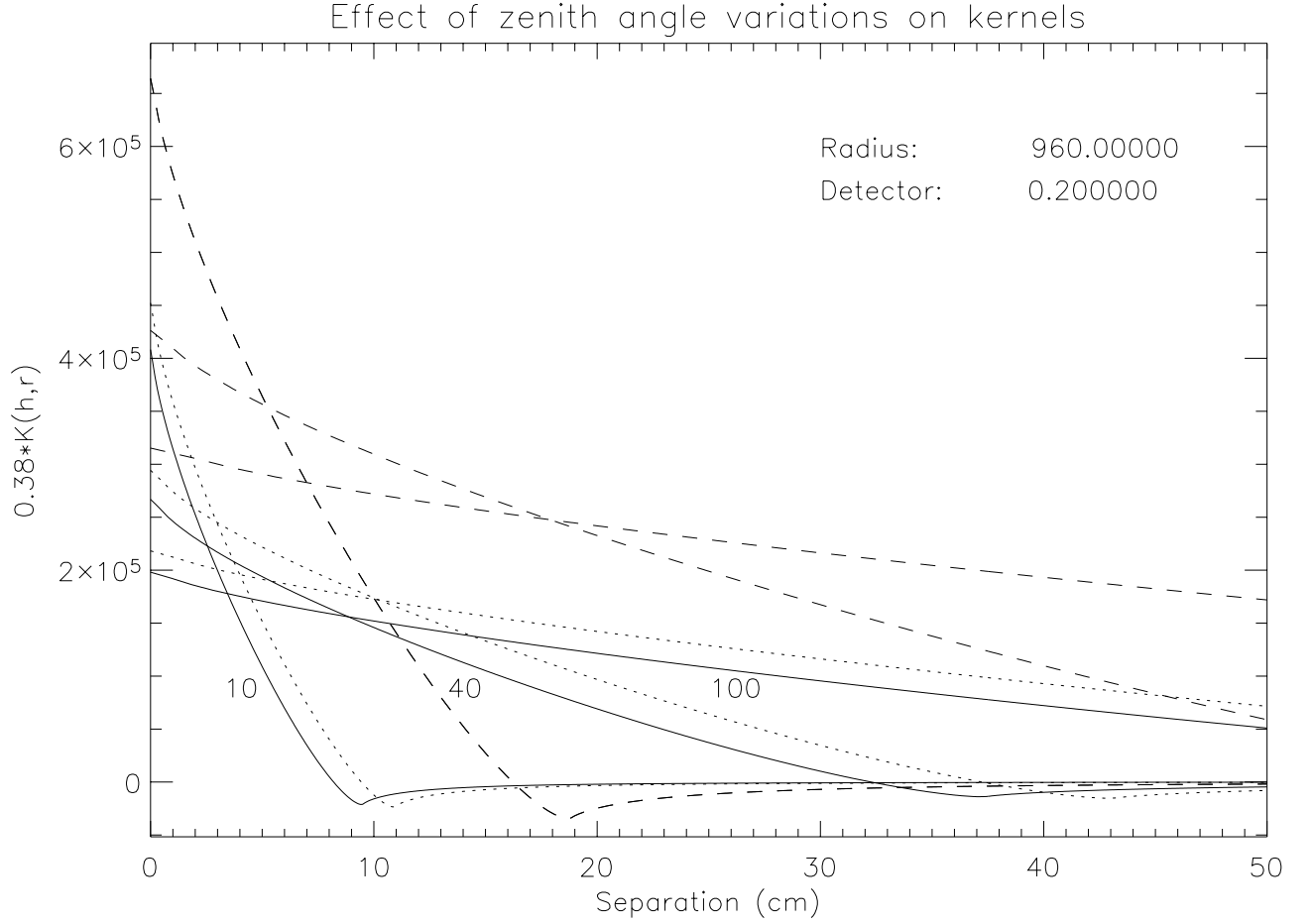


Fig. 8 The effect of a non-zero zenith angle on $0.38K(h, r)$. The function is shown for $\zeta = 0^\circ$ (solid line), 30° (dotted lines) and 60° (dashed lines) at three heights (10, 40, and 100 m). For this plot, $\theta = 960$ arcsec and $a = 0.2$ cm.

The advantage of this model is that it assumes nothing about the profile of $C_n^2(h)$ other than it can be sampled at selected heights. This avoids the introduction of systematic errors that generally result by fitting an inappropriate model to a data set.

3.2 Estimating $C_n^2(h)$

The next step is to determine the coefficients a_i . If the model is correct, then the observations B_j will differ from the model $B_I(r_j)$ by the observational noise alone. If σ_j is the estimate of the RMS uncertainty in the measured B_j then we can define an error E_m as

$$E_m = \frac{1}{n} \sum_{j=1}^n \sigma_j^{-2} (B_j - B_I(r_j))^2 \quad (43)$$

Thus, the task of estimating $C_n^2(h)$ should be accomplished in principle by choosing a_i such that E_m is minimized. In practice, this procedure is unstable, and additional constraints on the model must be applied. These constraints are usually motivated by prior physical knowledge of the process being modeled. In the case of $C_n^2(h)$, we know that it is a positive definite continuous function. In addition, we expect that the solution must be rather smooth, since we have essentially only 6 independent measurements from the SHABAR. We thus also apply a smoothing or regularization constraint by first defining E_s :

$$E_s^2 = \frac{1}{2q} \sum_{k=1}^q (\bar{y}_k - \bar{y}_{k-1})^2 \quad (44)$$

where

$$\bar{y}_k = \frac{1}{h_{k+1} - h_k} \int_{h_k}^{h_{k+1}} \ln C_n^2(h) dh \quad (45)$$

Then, the coefficients a_i are selected to minimize E , where

$$E = E_m + \Lambda E_s \quad (46)$$

and Λ is a regularization parameter that is adjusted to trade off the error and the height resolution of the estimated $C_n^2(h)$. In practice, the selection of a_i is accomplished using an amoeba optimization method. In addition, the minimization is done to compute $\ln C_n^2(h)$ so that $C_n^2(h)$ is positive definite.

Prior to the optimization, a height grid must be specified. There is no need to specify a very fine grid since there are a total of 15 covariance measurements and six independent detectors. In addition, the grid should place most of the height points at lower heights to accommodate the non-uniform sampling of the functions in Figure 5. Numerical experiments demonstrate that a small amount of oversampling is useful to reduce noise and stabilize the fit. We have thus adopted the following specification for the set of m heights which have a uniform separation Δh in $\log(h)$ up to a maximum height h_{\max} :

$$\Delta h = h_{\max}^{1/(m-1)} \quad (47)$$

Experiments have led to the choice of $m = 20$ and $h_{\max} = 10000$ meters.

Once the set of a_i has been determined, $C_n^2(h)$ can be computed and interpolated onto a fine grid to compute $r_0(h)$ via

$$r_0(h) = 0.18466\lambda^{6/5} \sec^{3/5} \zeta \left[\int_h^\infty C_n^2(h) dh \right]^{-3/5} \quad (48)$$

The fine grid is specified to have a spacing of 1 m from 0 to h_{\max} .

The data must be processed prior to applying the inversion procedure to obtain a set of estimated uncertainties σ_j . This is done by determining the mean and standard deviation of the mean of the covariances in a time block which has been chosen to be 5 minutes (30 samples). In addition, the observed covariances must be scaled by the scintillation signal in the detectors. This normalization constant and its uncertainty is obtained from the mean and standard deviation of the mean of the scintillation over all six detectors and in the 5-minute time block (total of 180 samples).

The code that produces the estimated $C_n^2(h)$ and $r_0(h)$ is provided in the Appendices. Appendix A contains the data preprocessing code. Appendix B provides the calculation of the kernel functions $K(h, r)$. The code that performs the inversion to determine $C_n^2(h)$ is provided in Appendices C and D.

4. Testing the method

In order to test the method, two approaches have been made. The first is to compute simulated profiles of $C_n^2(h)$ and then attempt to recover the input. The second test is experimental: obtain measurements from multiple SHABAR systems located at various physical heights, and compare $r_0(h)$ at the selected heights.

4.1 Constructing Simulated Profiles of $C_n^2(h)$

In order to test the different analyses, we construct synthetic profiles of $C_n^2(h)$. We start with computing the Huffnagel-Valley ($C_{nHV}^2(h)$) profile:

$$C_{nHV}^2(h) = A_{HV} \left[2.2 \times 10^{-23} \left(\frac{h+z}{1000} \right)^{-10} \exp\left(-\frac{h+z}{1000}\right) + 10^{-16} \exp\left(-\frac{h+z}{1500}\right) \right] \quad (49)$$

where A_{HV} is a chosen amplitude, and z is the elevation of the site in meters. The HV profile is a good approximation to $C_n^2(h)$ for night time conditions.

For a better model of a daytime $C_n^2(h)$, we add additional turbulence near the ground. The simulation allows three additional near-ground profiles:

- A simple exponential boundary layer:

$$C_n^2(h) = C_{nHV}^2(h) + A_B \exp(-h/h_0) \quad (50)$$

where A_B is the boundary amplitude and h_0 is the boundary scale height.

- A Valley boundary layer:

$$C_n^2(h) = C_{nHV}^2(h) + A_B(2.33 \times 10^{-15} + 5.38 \times 10^{-15} h^{-2/3}) \exp(-h/h_0) \quad (51)$$

- A Wyngaard boundary layer:

$$C_n^2(h) = C_{nHV}^2(h) + \frac{A_B}{h_0^{4/3} + h^{4/3}} \quad (52)$$

where here h_0 is a low cutoff to remove the singularity at $h = 0$.

The simulation also allows the addition of localized layers. These are specified with a height of the highest layer, the total number of layers, the mean and standard deviation of the layer thickness, and the mean and standard deviation of the layer strength relative to the background $C_n^2(h)$. The thickness and strength quantities are then used to generate a set of normally distributed layer properties that is added to $C_n^2(h)$.

Once the simulated $C_n^2(h)$ has been computed, it can be integrated to provide a simulated $r_0(h)$, and to compute a simulated $B_I(r_j)$. Random measurement noise is added, and the simulated observations can be inverted to estimate $C_n^2(h)$.

The results of this test are shown in Figures 9 and 10. Figure 9 shows that, in this specific realization, the method does a good job of providing a smoothed estimate of $C_n^2(h)$ at many heights but deviates from the input between $\log h = 2$ and $\log h = 3$. Figure 10 shows good agreement in $r_0(h)$ for heights up to 20 m, and then about a 10% overestimate higher up. The smoothing nature of the method is a result of the relatively small number of detectors in the system. Note that this is a single realization—the simulations should be run many times with different $C_n^2(h)$ profiles and with different observational noise realizations to build a Monte-Carlo statistical picture of the accuracy and precision of the method.

4.2 Observational multi-height test

In November 2001, we performed a test of the ability of the SHABAR to determine $r_0(h)$. This was done by placing three SHABAR systems at physically separate heights on and near the Dunn Solar Tower at Sacramento Peak. The systems were placed on a tripod on the ground, giving an effective height of 2 m; on the ATST Site Survey Test Stand putting the SHABAR at a height of 8 m; and on the top of the DST at a height of 40 m. The data from these 3 systems were then inverted. The results are shown in Figures 11 and 12, which compare the time history of r_0 from all three instruments at the common height of 40 m above the ground (38 m above the tripod instrument; 32 m above the test stand, and 0 m above the DST).

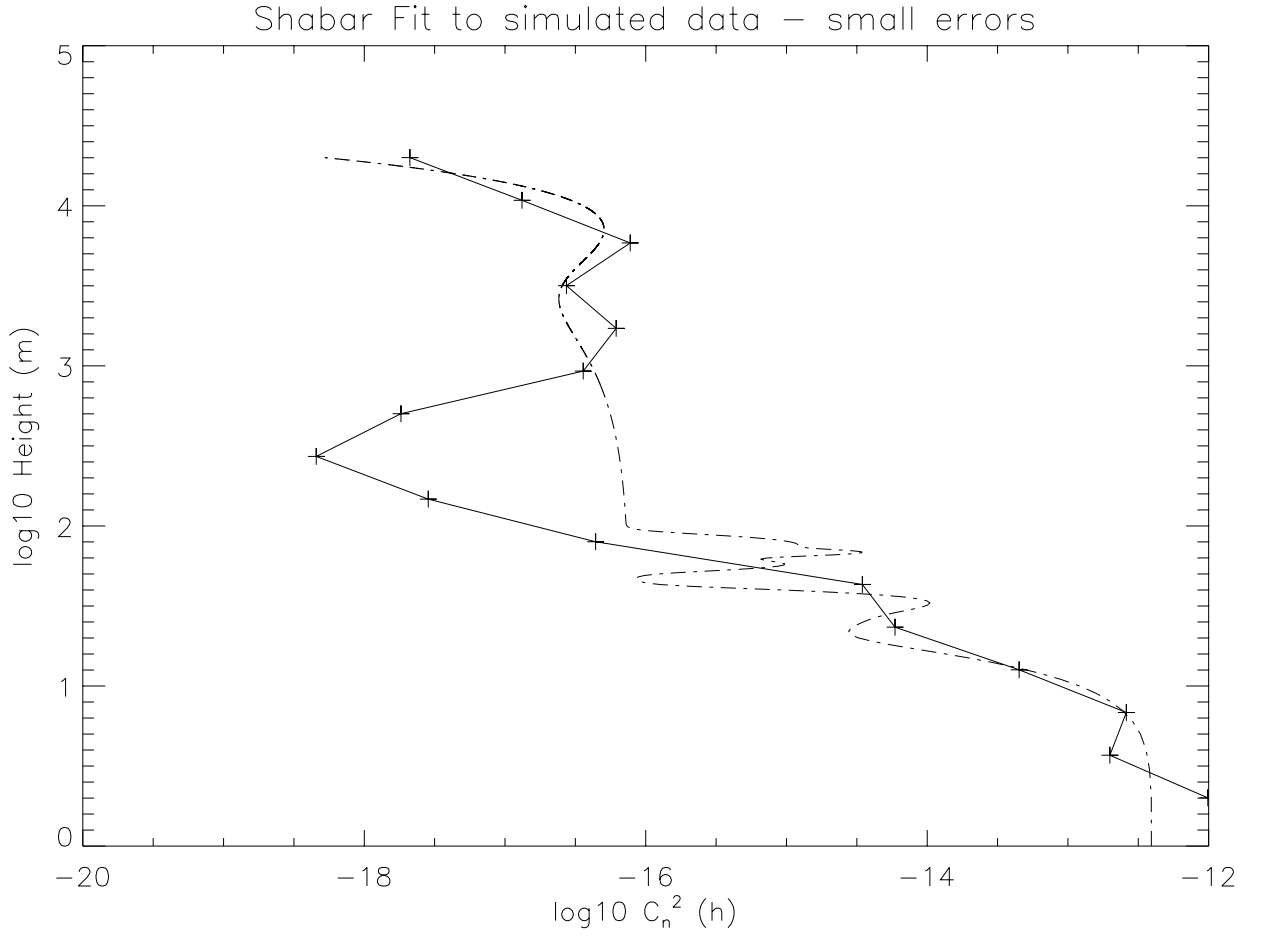


Fig. 9 A simulated $C_n^2(h)$ function (dash-dot line) and the inversion of the simulated data (solid line).

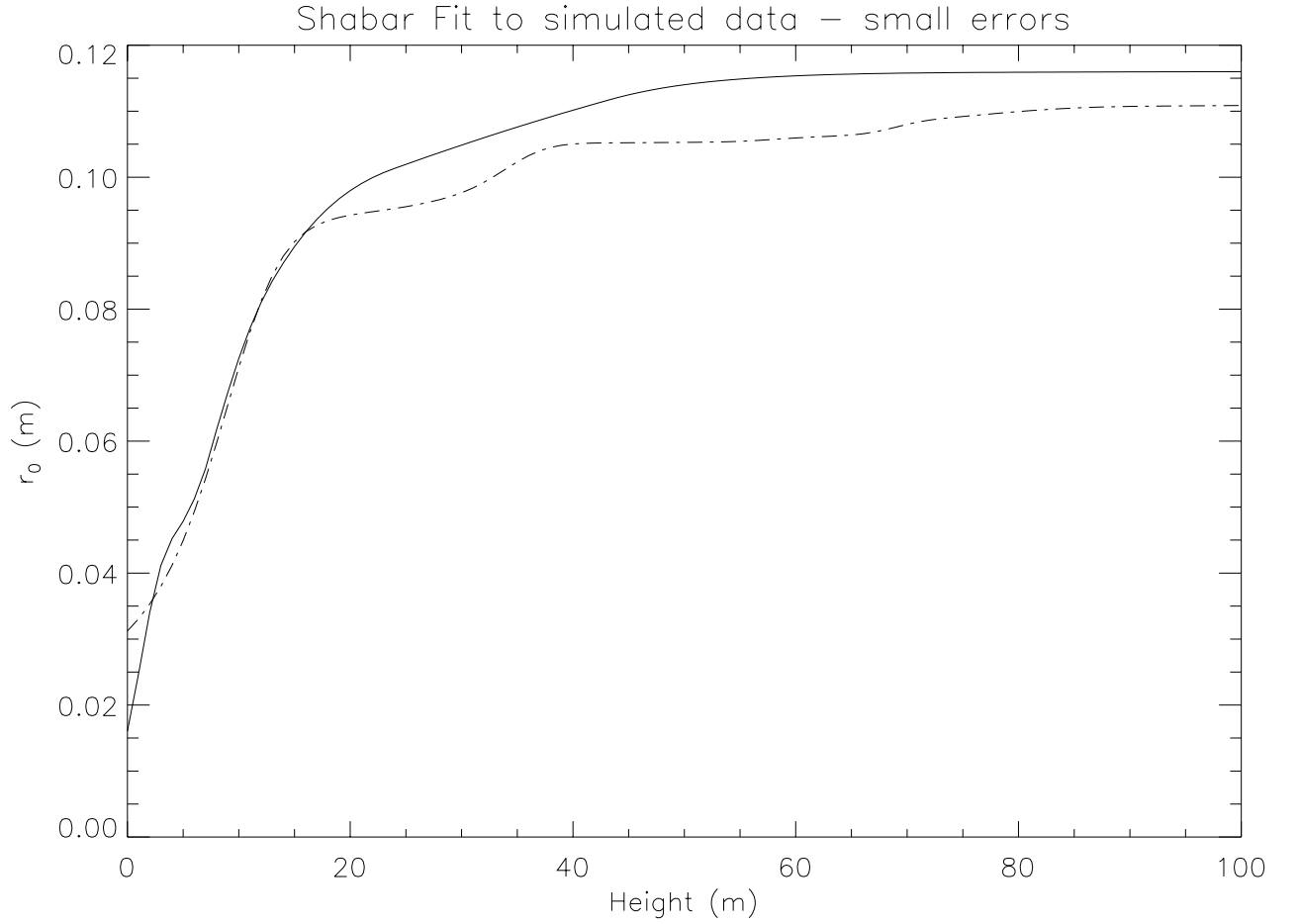


Fig. 10 The height profile $r_0(h)$ derived from the input simulated $C_n^2(h)$ function (dash-dot line) and the inversion of the simulated data (solid line).

Figure 11 shows the comparison using all data without regard for the operational status of the SHABARs. The agreement is generally very good, except at the beginning of the run, where several of the 40-m instrument values are substantially lower than the values from the other two instruments. In Figure 12, samples at which the instrument reported a problem with the SHABAR have been removed, the statistics within each 5-min time block have been renormalized for the varying number of valid data points, and only those blocks for which at least 25% of the points are valid have been retained. This shows that most of the discrepant points from the 40-m instrument were due to instrumental problems.

The results from both the simulations and the three-height test demonstrate that the inversion of the SHABAR data provides reasonably accurate estimates of $C_n^2(h)$ and $r_0(h)$. The method does not have enough resolution in height to capture narrow features in $C_n^2(h)$ but, as will be seen in the next section, can detect inversion layers in $C_n^2(h)$.

5. Applying the method to sample data

In this section, the inversion method is applied to short temporal sequences of SHABAR data obtained at three different sites. Site A is a continental mountain site, site B is a lake site, and site C is an ocean mountain peak. These three sites provide a range of different geographic and meteorological conditions, which potentially produce qualitatively different profiles of $C_n^2(h)$. Thus, this tests the response of the inversion method to diverse seeing conditions. In addition, another seeing instrument, a solar differential image motion monitor (S-DIMM) is colocated with the SHABAR on the same mount. The S-DIMM gives an independent measure of r_0 but only at the height of the mount, and weighted more heavily towards high layers in the atmosphere.

Figure 13 shows examples of the fits and the input data for the three sites. For site C (bottom figure), the observed covariance is negative for large separations, and the model does not fit the data well in this region. Since $\zeta > 60^\circ$ for this data, the poor fit may be an indication that the small perturbation approximation is invalid.

Figure 14 shows the set of inverted $C_n^2(h)$ for each of the sites, plotted with height on the y -axis so that layers can be seen in the correct orientation. Sites A and B show rather smoothly varying $C_n^2(h)$, while site C has a more chaotic nature. Site C also shows the appearance of inversion layers.

Figure 15 displays the temporal behavior of $C_n^2(h)$ at each of the heights sampled in the inversion. Site A shows an increasing $C_n^2(h)$ at all heights (top curves) until 17 UT when the higher layers appear to stabilize. Site B shows a fairly constant behavior of $C_n^2(h)$ over the short time analyzed, with large spikes at all heights which may be due to interference with the light entering the scintillometers. Site C shows a chaotic behavior at low heights, which vanishes in the upper layers.

Figure 16 compares the value of r_0 obtained from the S-DIMM and from the SHABAR at $h = 0$.

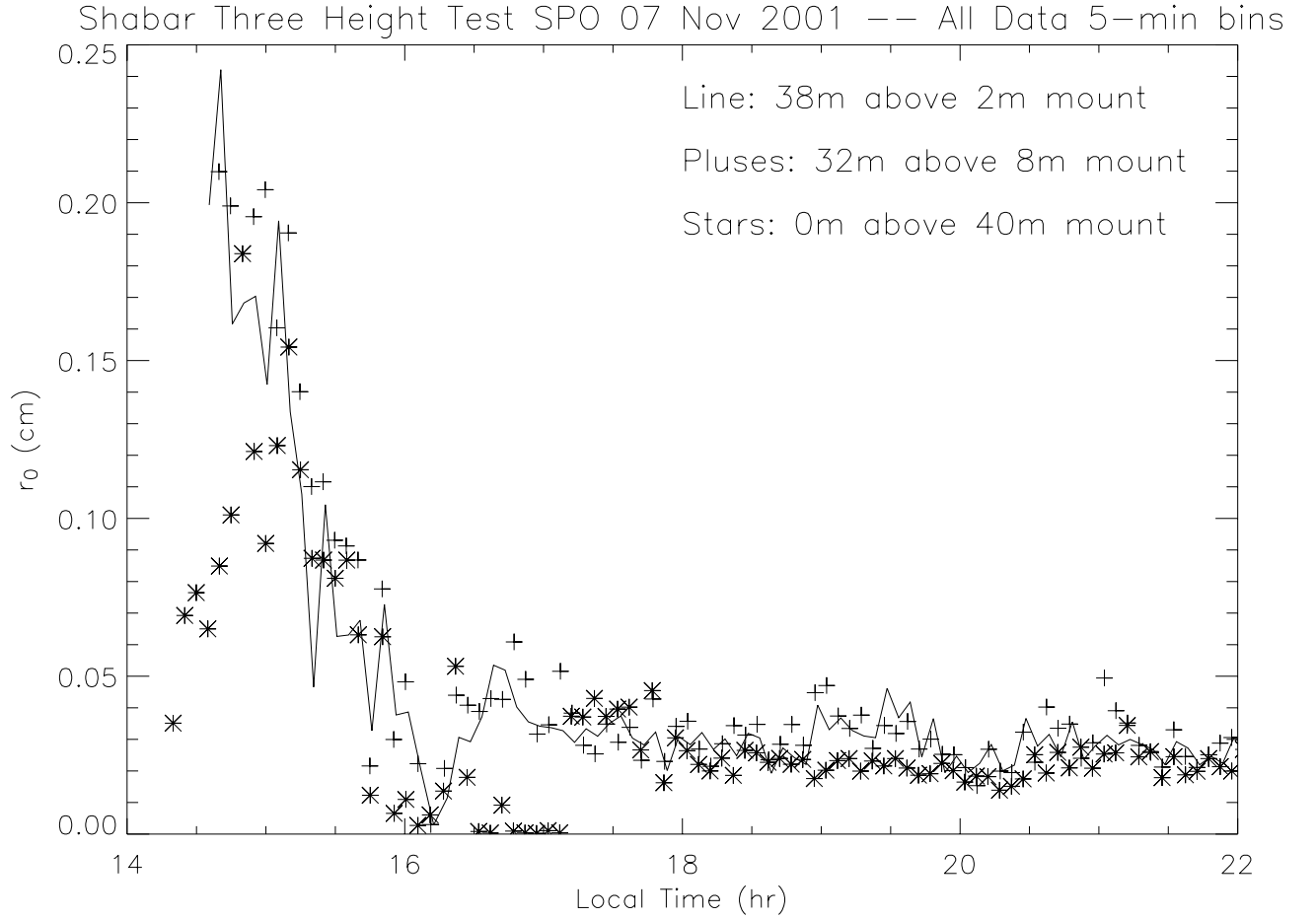


Fig. 11 The temporal variation of r_0 at a height of 40 m above the ground as obtained by inverting SHABAR data from three instruments mounted at heights of 2 (solid line), 8 (points marked with +), and 40 m (points marked with *). All data has been included in this plot.

Shabar Three Height Test SPO 07 Nov 2001 -- at least 25% Data 5-min bins

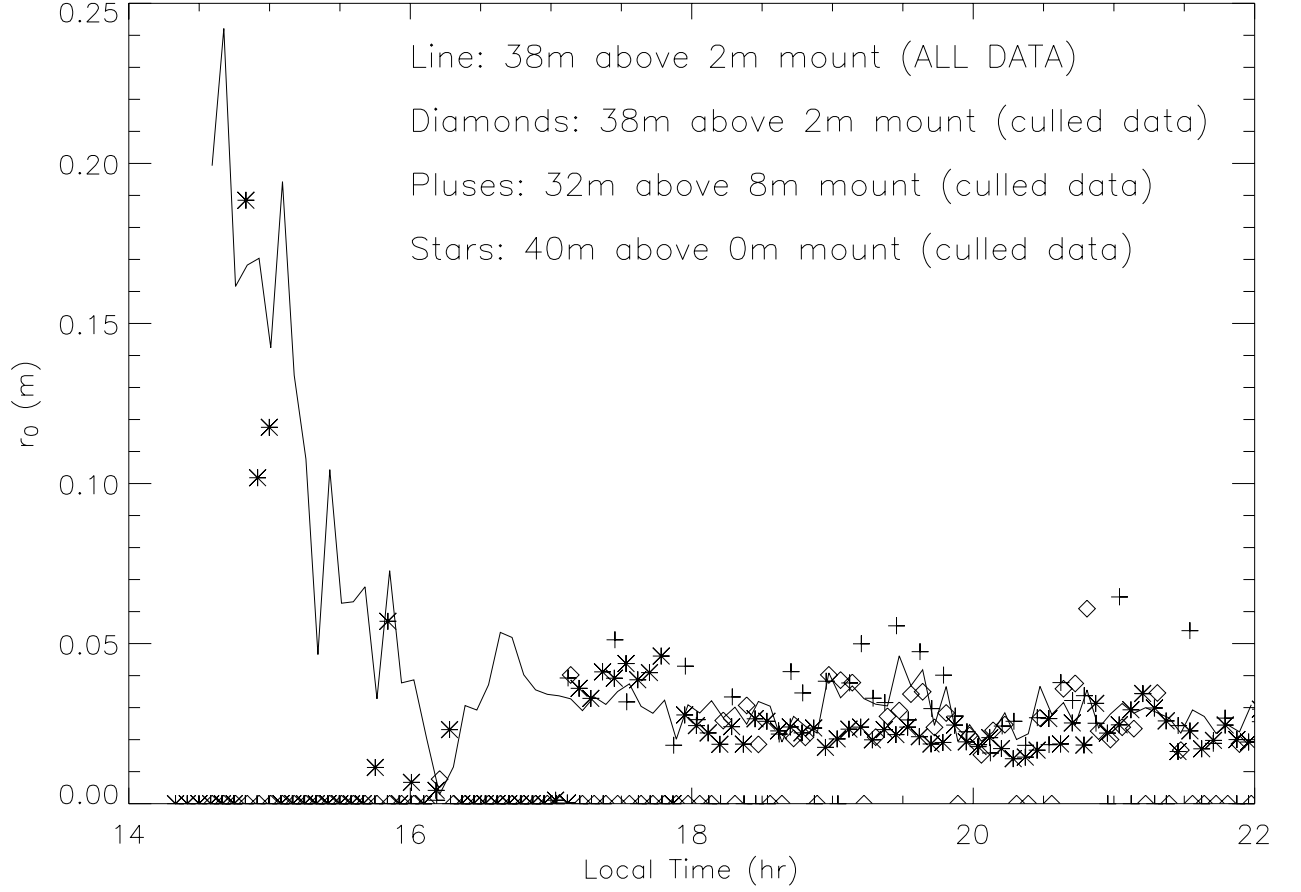


Fig. 12 As for Figure 11, but using culled data and including only those points for which at least 25% of the data points in a 5-min block were valid. Here, the solid line repeats the results for the instrument at 2 m including all data for reference. The points are for the culled data obtained at a height of 2 (points marked with a \diamond), 8 (points marked with +), and 40 m (points marked with *).

At Site A, these values track each other closely, implying that most of the seeing came from higher layers. Site B shows fairly poor agreement between the curves, with the SHABAR curve oscillating with a large amplitude. Since site B is a lake site, this may be an indication that the approximation that the contribution of humidity to $C_n^2(h)$ can be neglected is invalid. Site C shows a period of time when the two curves agree and then a period when the curves track each other but are offset. This suggests the formation of a low layer of turbulence as the day progresses.

Figure 17 shows the curves of $r_0(h)$ for various times at the sites. Sites A and B show similar smooth curves, and site C shows higher variability including one curve that has a plateau.

These plots demonstrate that $C_n^2(h)$ assumes very different qualities as a function of time and site. It will be very interesting to analyze many more data sets.

6. Conclusions

As discussed in section 2.2, there are approximations that have been made in the analysis that must be kept in mind—the results can be affected by the saturation of scintillation at large zenith angles, and the statistics of the turbulence could be altered by the presence of substantial humidity in the atmosphere. However, the SHABAR instrument is capable of providing $C_n^2(h)$ and $r_0(h)$ with sufficient accuracy over the first 100 m of height for the ATST site survey. This is demonstrated by the results in Figures 9 to 12.

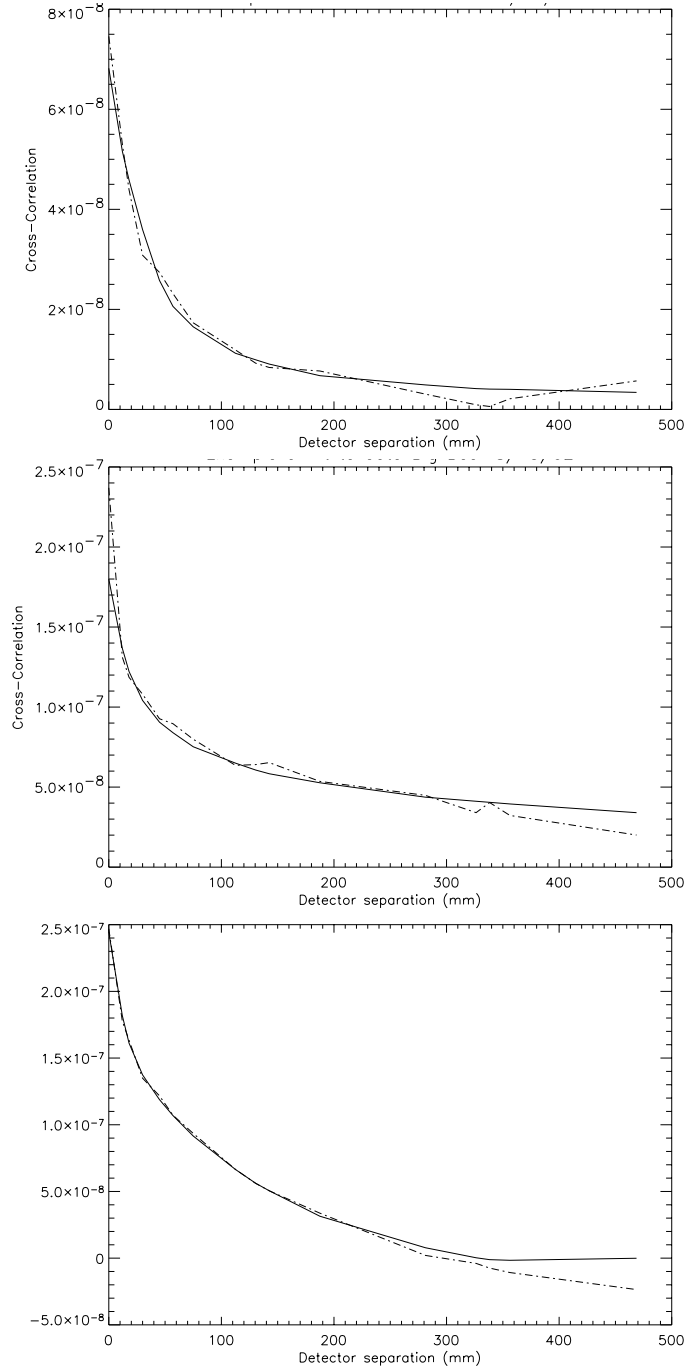


Fig. 13 The fit from the inversion (solid line) and the data (dash-dot line) for site A (top), B (middle), and C (Bottom)

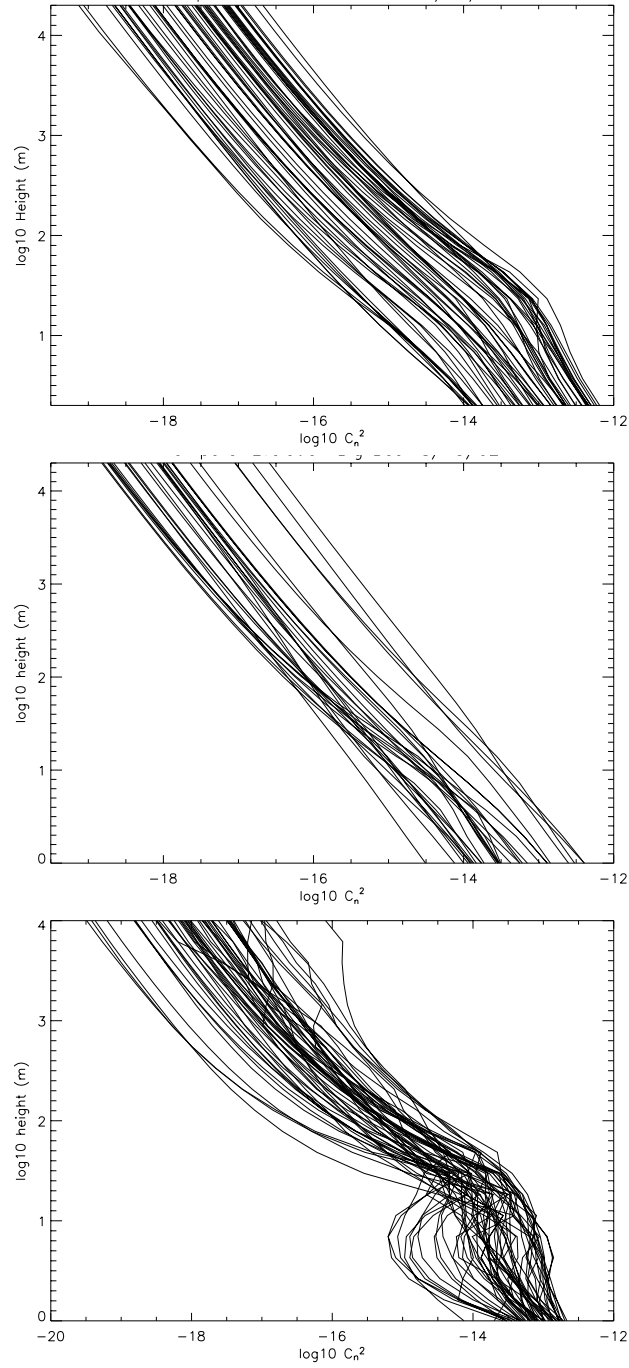


Fig. 14 The inverted $C_n^2(h)$ for site A (top), B (middle), and C (Bottom)

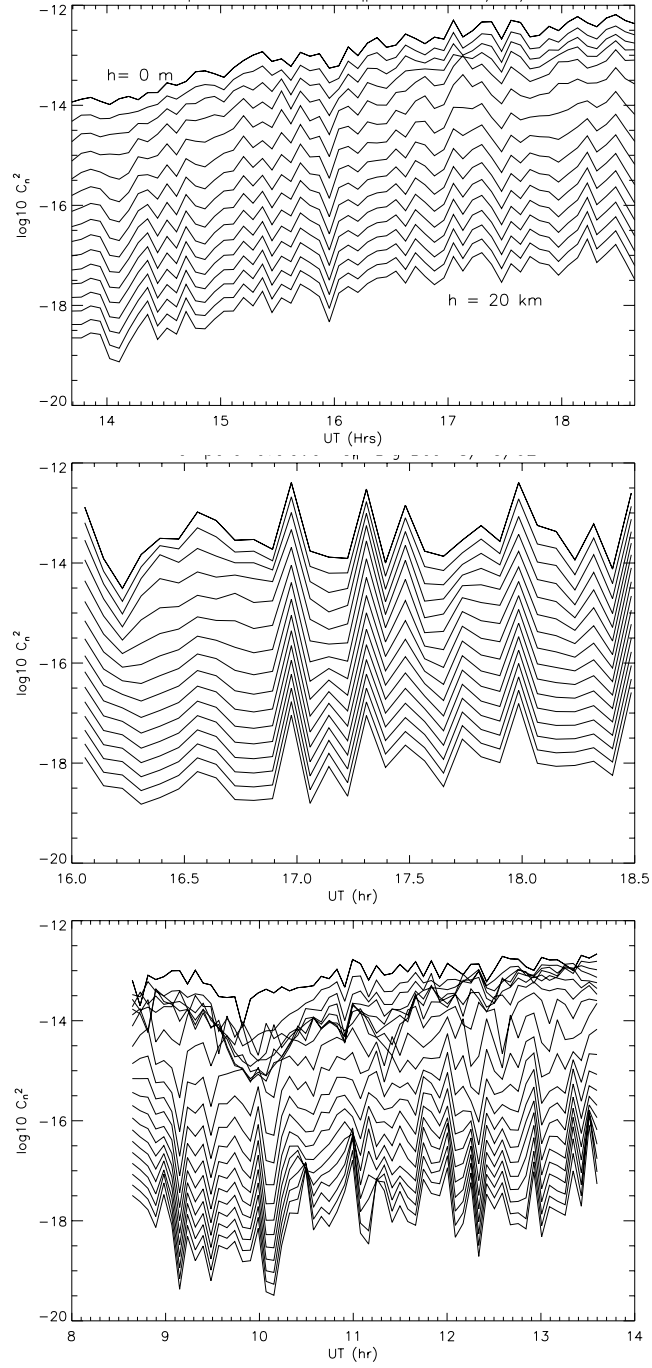


Fig. 15 The inverted $C_n^2(h)$ as a function of time for each height for site A (top), B (middle), and C (Bottom)

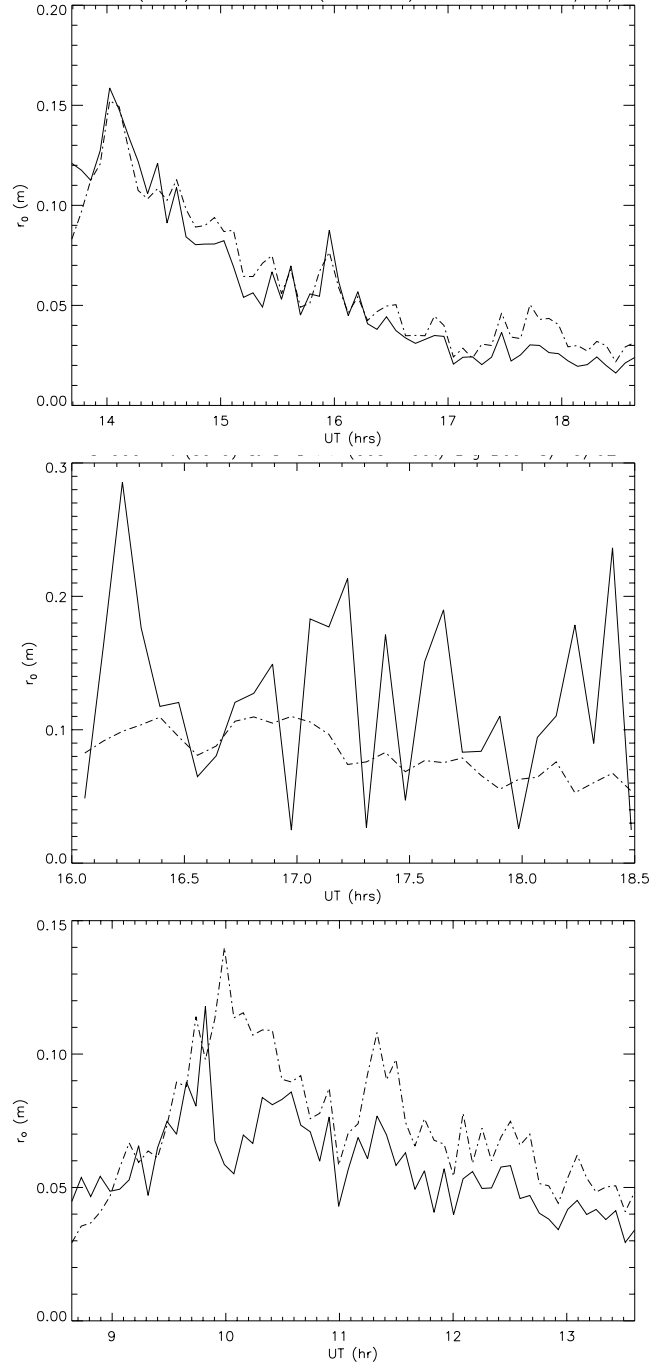


Fig. 16 Comparison of r_0 at $h = 0$ for the SHABAR (solid line) and the S-DIMM (dash-dot line) for site A (top), B (middle), and C (Bottom)

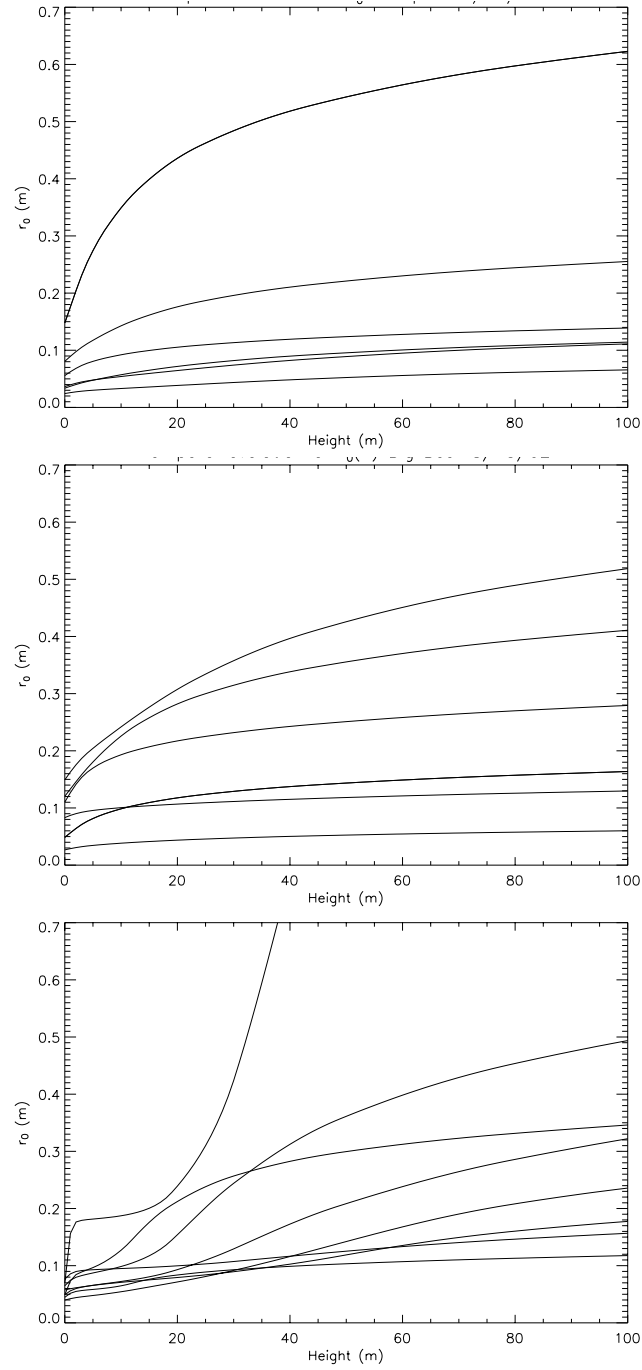


Fig. 17 Plots of $r_0(h)$ for various times for site A (top), B (middle), and C (Bottom)

Appendix A - The IDL data preprocessing procedure

```
pro procscint,ac,cc,t,tblock,data,errors,ndata,tdata
;
; procedure to pre-process the shabar scintillation data to prepare
; it for the inversion
; input: ac -- 2-D array of AC scintillation signals (npts,6)
;         cc -- 2-D array of scintillation cross-correlations (npts,15)
;         t -- array of times from the file
;         tblock -- the length of the time block, in sec, over which to
;                   compute the data statistics
; output: data -- the processed cross-correlations for input to the
;               inversion (ndata,16)
;         errors -- the corresponding error estimates
;         ndata -- the number of data points
;         tdata -- the time of each data point
;
; this routine multiplies the cross-correlations by the ac signal to
; recover a physical cross-correlation, and then
; computes the mean and variance of the cross-correlations over a length
; of time tblock sec.

dt=10. ; sampling rate in sec of original data.
ninp=n_elements(ac(*,0)) ; number of input points
nsamp = fix(tblock/dt) ; number of data points in each tblock time
fact=sqrt(float(nsamp)) ; for the sd of the mean
ndata = fix(ninp)/fix(nsamp) ; number of data points to be output
data=dblarr(ndata,16)
errors=dblarr(ndata,16)
tdata=dblarr(ndata)
acd=dblarr(ndata)
acde=dblarr(ndata)
; mapping of cc indices to separation order
ccsep=[11,12,13,14,15,4,5,6,10,1,3,9,2,8,7]
;
; compute the average and std. dev of the AC scintillation from all 6 detectors
; in a time block. This is the CC(0) signal.
```

```

;
for ib=0,ndata-1 do begin
    blst=ib*nsamp
    blnd=blst+nsamp-1
    rr=moment(ac(blst:blnd,*),sdev=errnow)
    acd(ib)=rr(0)
    acde(ib)=errnow
endfor
fact2=nsamp*6.0
data(*,0)=acd
errors(*,0)=acde/sqrt(fact2)
;errors(*,0)=acde
;
; compute the average and std dev of the cross-correlations
;
for ib=0,ndata-1 do begin
    blst=ib*nsamp
    blnd=blst+nsamp-1
    rt=moment(t(blst:blnd))
    tdata(ib)=rt(0)
    for icc=0,14 do begin
        ccnow=acd(ib)*cc(blst:blnd,icc)
        rr=moment(ccnow,sdev=errnow)
        data(ib,ccsep(icc))=rr(0)
        errors(ib,ccsep(icc))=errnow/fact
    ; errors(ib,ccsep(icc))=errnow
    endfor
endfor
return
end

```

Appendix B - The IDL kernel generating procedure

```
pro basisf2b,h,z,radius,x,func,q
;
; procedure to compute the basis functions for the ShaBar instrument
; for a given height at a given location at a given UT date & time
;
; input: h - height for basis function in meters
;        z,radius: zenith angle (deg) and solar radius (arcsec)
;        x - an array of detector separations in cm
; NOTE: either h OR x can be an array, but not both!
; output:func - array containing the basis function. It is either an
; array for all h at a given x, or for all x at a given h, depending on
; the input.
z=double(z)
radius=double(radius)
close,3
openr,3,'/enz0/hill/atst/cn2h/qsbest.dat'
q=dblarr(2001)
readf,3,q
close,3
s=dindgen(2001)*0.01d0
adet=0.2d0 ; detector diameter in cm
cz=cos(z*double(!DTOR)) ; cosine (zenith angle)
sz=1.d0/cz ; secant (zenith angle)
omega=(2.d0*radius/3600.d0)*double(!dtor) ; solar diameter in radians
alpha=2.d0*tan(omega/2.d0) ; the factor relating physical to angular diameter
;print,' zenith angle: ',z
;print,' alpha: ',alpha,' omega:',omega
;
; compute kernel function
ze=adet*.01d0+alpha*h*sz
num=32.d0*!dpi*h*h*sz*sz*sz
denom=ze^(7.d0/3.d0)
fact=num/denom
;print,' ze: ',ze,' fact: ',fact
; interpolate
```

```
xm=x*.01d0 ; convert to meters
sn= xm/ze
rr=interp(q,s,sn)
func=rr*fact
return
end
```

Appendix C - The IDL inversion procedure

```
pro invcn2hb,data_arr,errors,zen,radius,lambdat,ni,solution,hhs,model,r0,$
    lmf,ferr,serr,nit
;
; procedure to invert the Shabar covariance data to infer
; cn2(h)
;
; input: data is the set of 15 covariances between the detector pairs
;        error is the array of 15 estimated errors in the data
;        zen, radius: zenith angle (degrees) and solar radius (arcsec)
common func_f,error,data,krn,hh,lambda,err1,err2
data=double(data_arr)
error=double(errors)
lambda=double(lambdat)
;
; set up array of detector separations in mm
dist=dblarr(6)
sep=dblarr(16)

dist(5)=-234.375D
dist(4)=-121.875D
dist(3)=-103.875D
dist(2)= -91.875D
dist(1)= -46.875D
dist(0)= 234.375D

sep(00)=0.0D
sep(01)=dist(2)-dist(3)
sep(02)=dist(3)-dist(4)
sep(03)=dist(2)-dist(4)
sep(04)=dist(1)-dist(2)
sep(05)=dist(1)-dist(3)
sep(06)=dist(1)-dist(4)
sep(07)=dist(4)-dist(5)
sep(08)=dist(3)-dist(5)
sep(09)=dist(2)-dist(5)
```

```

    sep(10)=dist(1)-dist(5)
    sep(11)=dist(0)-dist(1)
    sep(12)=dist(0)-dist(2)
    sep(13)=dist(0)-dist(3)
    sep(14)=dist(0)-dist(4)
    sep(15)=dist(0)-dist(5)
nsep=16
;
; set up array hh of heights in meters
;
;nh=0.5*nsep
nh=20
dh=10000.d0^(1.d0/(nh-1))
ddh=sqrt(dh)-1.d0/sqrt(dh)
ht=dindgen(nh)
hh=1.d0*dh^ht
;hh(nsep)=20000.d0
nh=n_elements(hh)
;
; set up the array of kernels
;
krn=dblarr(nh,nsep)
for ih=0,nh-1 do begin
    basisf2b,hh(ih),zen,radius,sep*0.1,f
    krn(ih,*)=0.38d0*f(*)
endfor
krns=krn
; The model is to represent cn2(h) as a sum of Dirac delta functions
; at the heights in hh
;
p0=alog(data(0)/krn(*,0))
p0=reform(p0)
scale=20.d0
ftol=1.d-5
tol2=1.d-1
tol3=100.d0
;print,p0
r=amoeba(ftol,scale=scale,p0=p0,function_name='cn2func',$

```

```

        ncalls=niter,function_value=fval,nmax=2000000)
;print,'r: ',r
;print,'niter: ',niter,' fval: ',fval
;goto,done
ii=0
again:bb=0
ii=ii+1
rprev=r
r=amoeba(ftol,scale=scale,p0=rprev,function_name='cn2func',$
        ncalls=niter,function_value=fval,nmax=2000000)
;print,'r: ',r
;print,'ii: ',ii,' niter: ',niter
dif=sqrt(total((r-rprev)^2)/nh)
;print,' lambda: ',lambda,' dif: ',dif
;print,' err1: ',err1,' err2' ,err2
;if (dif le tol2)then goto, done
if (err1 le tol2 and err2 le tol2 or ii ge ni)then goto, done
;if (dif ge tol3 or ii eq ni)then begin
;  lambda=1.1*lambda
;  goto, again
;endif
if (err2 lt err1 )then lambda=lambda/1.1 else lambda=lambda*1.1
  goto, again
done:solution=r-alog(hh*ddh)
hhs=hh
nn=n_elements(data)
model=dblarr(nn)
for j=0,nn-1 do model(j)=total(exp(r)*krn(*,j))
;dneg=where(data lt 0,icnt)
;if(icnt ne 0) then model(dneg)=-1.*model(dneg)
;stop
lam=5.d2 ; wavelength in nm
lam=lam*1.d-9 ; convert to m
lam2=lam^(-2.d0)
cz=cos(zen*double(!DTOR)) ; cosine (zenith angle)
sz=1.d0/cz ; secant (zenith angle)

const=16.6d0*lam2*sz

```



```

;r0=dblarr(nh-1)
;for ih=0,nh-2 do r0(ih)= $
;  int_tabulated(hhs(ih:nh-1),exp(solution(ih:nh-1)),/double)
;r0=const*r0
;r0=r0^(-3.d0/5.d0)
;
hhi=dindgen(20001)
hhi=dindgen(max(hhs)+1)
cn2h=interpol(alog10(exp(solution)),hhs,hhi)
cn2h=10.^cn2h
r0=0.18466*lam^(6./5.)*cz^(3./5.)*(total(reverse(reform(cn2h)),/cumulative))^(-3./5.)
r0=reverse(r0)

ferr=err1
serr=err2
lmf=lambda
nit=ii
return
end

```

Appendix D - The IDL minimization function procedure

```
function cn2func,a
common func_f,errors,data,kernels,hh,lambda,t1,t2

nn=n_elements(data)
nh=n_elements(hh)
model=dblarr(nn)
q=nh-1

for j=0,nn-1 do model(j)=total(exp(a)*kernels(*,j))
;dneg=where(data lt 0,icnt)
;if (icnt ne 0)then model(dneg)=-1.*model(dneg)
t1=(1./nh)*total(((data-model)/errors)^2)

dh=ts_diff(hh,1)
da=ts_diff(a,1)
;t2=(1.d0/(2.d0*q))*total((da(0:q-1)/dh(0:q-1))^2.d0)
t2=(1./(2.*q))*total(da(0:q-1)^2.)
;rint,'t1: ',t1,' t2: ',t2,' func: ',t1+lambda*t2
return,t1+lambda*t2
end
```

References

- Beckers, J. M. 1993, *Solar Phys.* **145**, 399.
- Beckers, J. M. 1999, *Third Advances in Solar Physics Euroconference: Magnetic Fields and Oscillations*, ed. B. Schmieder, A. Hofmann & J. Staude, *ASP Conf. Series* **184**, 309.
- Beckers, J. M. 2001, *Experimental Astron* **12**, 1.
- Beckers, J. M., Leon, E., Mason, J., and Wilkins, L. 1997, *Solar Phys.* **176**, 23.
- Beckers, J. M., Liu, Z., and Jin, Z., 2003, *Innovative Telescopes and Instrumentation for Solar Astrophysics*, ed. S. Keil & S. V. Avakyan, *Proc. SPIE* **4853**, 273.
- Beckers, J. M., and Rutten, R. J. 1998, *New Astron. Rev.* **42**, 489.
- Radick, R.R., Briggs, J. W., Fletcher, S., and Hegwer, S. 2002, *Bull. Astron. Soc. Am* **34**, 734.
- Roddier, F. 1981, *Progress in Optics* **19**, 281.
- Seykora, E. J. 1993, *Solar Phys.* **145**, 389.